UC Riverside
UC Riverside Previously Published Works

Title

Degradation of Bioresorbable Mg–4Zn–1Sr Intramedullary Pins and Associated Biological Responses in Vitro and in Vivo

Permalink

https://escholarship.org/uc/item/5dn3m7qz

Journal

ACS Applied Materials & Interfaces, 9(51)

ISSN

1944-8244

Authors

Cipriano, Aaron F
Lin, Jiajia
Lin, Alan
et al.

Publication Date

2017-12-27

DOI

10.1021/acsami.7b15975

Peer reviewed

Degradation of Bioresorbable Mg–4Zn–1Sr Intramedullary Pins and Associated Biological Responses in Vitro and in Vivo

Aaron F. Cipriano[†,‡], **Jiajia Lin**[‡], **Alan Lin**[†], **Amy Sallee**[†], **Belinda Le**[†], **Mayra Celene Cortez Alcaraz**[†], **Ren-Guo Guan**[§], **Gary Botimer**[∥], **Serkan Inceoglu**[∥], and **Huinan Liu**[†,‡,⊥,#,*]

[†]Department of Bioengineering, University of California, Riverside California 92521. United States

[‡]Materials Science & Engineering, University of California, Riverside California 92521. United States

[§]School of Materials Science and Engineering, Northeastern University, Shenyang 110819. China

[∥]Department of Orthopedic Surgery, Loma Linda University, Loma Linda, California 92354. United States

[⊥]Stem Cell Center, University of California, Riverside California 92521. United States

[#]Cell, Molecular and Developmental Biology Program, University of California, Riverside California 92521. United States

Abstract

This article reports the degradation and biological properties of as-drawn Mg–4Zn–1Sr (designated as ZSr41) and pure Mg (P–Mg) wires as bioresorbable intramedullary pins for bone repair. Specifically, their cytocompatibility with bone marrow derived mesenchymal stem cells (BMSCs) and degradation in vitro, and their biological effects on peri-implant tissues and in vivo degradation in rat tibiae were studied. The as-drawn ZSr41 pins showed a significantly faster degradation than P–Mg in vitro and in vivo. The in vivo average daily degradation rates of both ZSr41 and P–Mg intramedullary pins were significantly greater than their respective in vitro degradation rates, likely because the intramedullary site of implantation is highly vascularized for removal of degradation products. Importantly, the concentrations of Mg^{2+}, Zn^{2+}, and Sr^{2+} ions in the BMSC culture in vitro and their concentrations in rat blood in vivo were all lower than their respective therapeutic dosages, i.e., in a safe range. Despite of rapid degradation with a complete resorption time of 8 weeks in vivo, the ZSr41 intramedullary pins showed a significant net bone growth because of stimulatory effects of the metallic ions released. However, proportionally released OH^- ions and hydrogen gas caused adverse effects on bone marrow cells and resulted in cavities in surrounding bone. Thus, properly engineering the degradation properties of Mg-based implants is critical for harvesting the bioactivities of beneficial metallic ions, while controlling adverse reactions associated with the release of OH^- ions and hydrogen gas. It is necessary to

[*]Corresponding Author: Address: 900 University Avenue Riverside, CA 92521. Office: MSE 227. Phone: 951 827 2944. Fax: 951 827 6416. huinan.liu@ucr.edu.
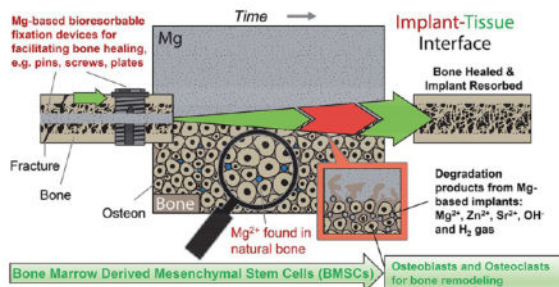
ORCID

Huinan Liu: 0000-0002-7479-7273

further optimize the alloy processing conditions or modify the surfaces, for example, applying coatings onto the surface, to reduce the degradation rate of ZSr41 wires for skeletal implant applications.

Graphical Abstract

Keywords

biodegradable magnesium zinc strontium (Mg–Zn–Sr) alloy; bioresorbable intramedullary pin implant in rat tibia; biodegradation in vitro and in vivo; cytocompatibility and biocompatibility; bone remodeling; microcomputed tomography (microCT or μCT)

1. INTRODUCTION

Magnesium (Mg) is the basis of a novel class of metallic biomaterials that has attracted growing attention for its advantageous properties for medical applications: (1) it has the needed modulus and mechanical strength that closely match load-bearing bones; (2) it is biodegradable, and its degradation products can be safely metabolized and eliminated through urine when the rate of degradation is modulated to a desirable range. Recent progress in the alloy design, processing, and manufacturing technologies has provided new opportunities for Mg-based biodegradable metals in even broader applications. Mg-based alloys have been actively studied for biomedical applications since the early 2000s.[1–3] Mg alloys could provide the combined advantages of traditional metallic and polymeric materials and overcome their disadvantages, when the composition, processing, microstructure, and surface of the materials are engineered properly for medical implant applications. The physical, mechanical, electrochemical, and biological properties of Mg alloys make them promising biomaterials for making temporary implants that can degrade and disappear after serving their functions in the body.[1–4] Biodegradable metallic implants could eliminate the need for implant removal surgeries following healing of the damaged tissues and thus reduce the burden on the healthcare system by mitigating risks and costs.[5,6]

The key challenge is to control the degradation and bioactivity at the tissue-implant interface to take full advantage of Mg-based metals for medical use. When engineering the degradation rate of Mg-based biomaterials, it is critical to target the end-goal applications and consider the application-specific design criteria. Crystalline magnesium–zinc–strontium (Mg–Zn–Sr) ternary alloys consist of elements naturally present in the human body and provide attractive mechanical and biodegradable properties for a variety of biomedical

applications.[7–11] Zn has a maximum solubility of 6.2 wt % as an alloying element in Mg and improves the mechanical properties and corrosion resistance through solid solution strengthening and age hardening.[7] When alloying Sr in Mg, intermetallic compounds form and induce grain refinement, which improves the mechanical properties and corrosion resistance.[7] Previously, the as-rolled Mg–4Zn–1Sr (designated as ZSr41) alloy sheet showed an ultimate tensile strength of 270 MPa and elongation at failure of 12.8%, greater than the as-rolled pure Mg control that showed an ultimate tensile strength of 197.1 MPa and elongation at failure of 10.3%.[7] From the bioactivity perspective, Mg–Zn–Sr alloys contain 3 nutrient elements that serve natural functions in the body and provide beneficial effects for bone repair. Zn plays an important role in activities of more than 100 enzymes, protein synthesis, immune function, and wound healing.[12–15] If Zn becomes deficient in the body, DNA replication slows and protein synthesis is restrained.[16] Sr is a natural component in bones and can promote osteoid formation and bone growth.[17,18] Low doses of stable Sr compounds promote bone synthesis and metabolism, and are clinically used to promote osteoid formation and treat osteoporosis.[18–21] When alloying Sr in Mg, Mg–1Sr alloy promoted osteogenic activities in vivo by controllable release of Sr.[22] The composition, processing, microstructure, and mechanical properties of Mg–4Zn–xSr ternary alloys, and the associated degradation and biological performance in different physiologically relevant in vitro culture systems have been reported previously.[7–11] The in vitro model systems are valuable for initial screening of cytocompatibility and cytotoxicity of engineered biomaterials,[23,24] and in vivo evaluations at a later-stage of biomaterial development remain imperative for clinical translation. Particularly for Mg alloys, the differences between the results from in vitro versus in vivo studies require special attention.[25–27] Therefore, the Mg–4Zn–1Sr (i.e., ZSr41) alloy was fabricated into the form of intramedullary pins and their degradation and biological performance in vitro and in vivo were investigated in this study.

Specifically, the first objective of this study was to investigate the in vitro degradation and cytocompatibility of ZSr41 intramedullary pins in exposure culture with bone marrow derived mesenchymal stem cells (BMSCs) in Dulbecco's Modified Eagle Medium (DMEM). The BMSC/DMEM culture system was used because the previous results indicated that Mg degradation in this in vitro system resembled in vivo conditions closely with the presence of physiologically relevant ions, proteins, and cells.[28–31] Furthermore, BMSCs play important roles in early implant osseointegration and bone regeneration,[32] and are highly relevant for testing the cytocompatibility of Mg-based biomaterials for orthopedic applications.[24,33] The second objective of this study was to investigate for the first time the in vivo degradation of ZSr41 intramedullary pins and associated biological responses when implanted in a rat tibia model. The methods for measuring in vitro degradation (electrochemical and immersion) and in vivo degradation (microcomputed tomography in situ) of ZSr41 and pure Mg intramedullary pins were carefully selected so that the results can be directly compared with published literature.[27] Overall, this study contributes to the field-wide efforts[25–27] on addressing the gaps between in vitro and in vivo degradation of Mg-based metals for medical implant applications, and enhance our understanding on the biodegradation of Mg-based implants and associated biological responses for skeletal implant applications.

2. MATERIALS AND METHODS

2.1. Preparation of ZSr41 Alloy and Mg Pins

The ZSr41 alloy had a nominal composition of 4 wt % Zn and 1 wt % Sr in a Mg matrix. The ZSr41 alloy intramedullary pins were produced by a metallurgical process consisting of melting, casting, extrusion, drawing, and heat treatment. First, high-purity commercially available Mg ingots (99.94 wt %; Boyu, Shenyang, China) were melted at 750 °C using a steel crucible under a gas-protected environment consisting of Argon (Ar) and 2% SF_6. Subsequently, commercially available bulk metallic Zn (99.5%; Boyu, Shenyang, China), and a Mg–20 wt % Sr master alloy (Boyu, Shenyang, China) were added to the melt at 720 °C in the nominal amounts to achieve the composition of 95 wt % Mg, 4 wt % Zn, and 1 wt % Sr. The mixture was stirred (30 min, 200 rpm) and heated for 15 min at 700 °C to homogenize and deslag the melt. The melt was cast as ingots (Ø30 × 150 mm) at 700 °C and solidified in the air. After they were cast, 25 mm from either end of the ingots (lengthwise) were removed and the middle segments (100 mm in length) underwent solution heat treatment at 450 °C for 12 h, followed by quenching in water. Subsequently, the heat-treated ingots were hot extruded at 250 °C to produce ZSr41 wires with a diameter of 4 mm; the extrusion ratio was 56.25:1 (i.e., from the diameter of 30 mm to 4 mm, 7.5^2). Lastly, the hot-extruded wires with a diameter of 4 mm were drawn through multiple passes at 150 °C with a drawing ratio of 1.44:1 to produce ZSr41 wires with a diameter of 1.1 mm; the intermediate diameters were Ø3.3, Ø2.8, Ø2.3, Ø1.9, Ø1.6, and Ø1.3. The work pieces were heat treated at 300 °C for 30 min after each drawing pass to remove residue stress. Commercially pure Mg wire (P–Mg; 99.9+%, as-drawn, catalog no. 679-751-72; Goodfellow Co., Coraopolis, PA, USA) with a nominal diameter of 1.1 mm (1.05 ± 0.03 mm measured) was used as a control in this study. The as-drawn ZSr41 alloy and P–Mg wires were cut into 15.08 ± 0.46 mm long intramedullary pins, polished with SiC abrasive papers (Ted Pella Inc., Redding, CA, USA) up to 1200 grit, ultrasonically cleaned in separate baths of acetone and 200-proof ethanol for 15 min each, individually weighed (M_0), and sterilized using an autoclave at a standard gravity cycle (122 °C for 30 min). It is necessary to sterilize each sample before its use for in vitro cell culture and in vivo implantation.

2.2. Surface Characterization of ZSr41 Alloy and Mg Pins

Prior to electrochemical tests, and in vitro and in vivo experiments, the surface microstructure of ZSr41 and P–Mg pins were characterized before and after sterilization using a scanning electron microscope (SEM; Nova NanoSEM 450, FEI Co., Hillsboro, OR, USA). The samples were designated as either polished or autoclaved; the former was immediately after polishing and the latter consisted of polishing followed by sterilization through autoclaving. Surface elemental composition and distribution were analyzed with energy dispersive X-ray spectroscopy (EDS) using a Nova NanoSEM 450 equipped with an X-Max50 detector and AZtecEnergy software (Oxford Instruments, Abingdon, Oxfordshire, UK). An accelerating voltage of 20 kV was used to obtain SEM images and perform EDS analysis. Additionally, X-ray diffraction (XRD; Empyrean, PANalytical, Westborough, MA, USA) was used to analyze the crystal structures of the phases present. All XRD spectra were acquired using Cu Kα radiation (45 kV, 40 mA) at a step size of 0.006°, and dwell time of 50 s using a PIXcel 1D detector (PANalytical). Phase identification was performed using the

HighScore software (PANalytical) and were identified according to the standard patterns in the Inorganic Crystal Structure Database (ICSD): 01-089-7195 for Mg, 01-074-6807 for $Mg_{17}Sr_2$, 00-001-1185 for Mg_7Zn_3, 01-075-9570 for MgO, 01-078-3960 for $Mg(OH)_2$, 01-076-8940 for $(Mg_{0.25}Zn_{0.75})O$, and 01-075-0263 for SrO.

2.3. Electrochemical Testing of ZSr41 Alloy and Mg Pins

Potentiodynamic polarization (PDP) curves were obtained using a potentiostat (Model 273A, Princeton Applied Research, Oak Ridge, TN, USA) with a three-electrode cell configuration and acquired with the PowerSuite 2.50.0 software (Princeton Applied Research). Specific details pertaining to preparation of the working electrode are given elsewhere.[10,24] Briefly, the polished ZSr41 and P–Mg pins were embedded longitudinally in epoxy resin as the working electrode and then ground with SiC abrasive paper to expose a rectangular cross section along the length of the pin (0.17 cm^2 exposed). Platinum foil was used as the counter electrode, and a silver/silver chloride (Ag/AgCl) electrode was used as reference. Prior to electrochemical experiments, the working electrode was polished and cleaned as described above but not autoclaved. Revised simulated body fluid (r-SBF; pH 7.4, 37.5 °C) was used as the electrolyte, because the ionic composition of r-SBF is the same as human blood plasma. The PDP scans were from 0.5 to –3.5 V at a scan rate of 20 mV s^{-1}. Values for corrosion potential (E_{corr}) and corrosion current density (J_{corr}) were extrapolated from the PDP curves using the Tafel method according to ASTM G102–89 standard. All potentials were measured in reference to Ag/AgCl electrode.

2.4. Cytocompatibility and Degradation of ZSr41 Alloy and Mg Pins in Exposure Culture with BMSCs in Vitro

BMSCs were harvested from the femur and tibia of a three-week-old female Sprague–Dawley rat following the protocol approved by the Institutional Animal Care and Use Committee (IACUC) at the University of California, Riverside (UCR). Specific details regarding BMSC extraction, isolation and culture are described elsewhere.[34] Briefly, the distal and proximal ends of the bones were dissected and the bone marrow was flushed out of the bone cavity and collected using DMEM (Sigma-Aldrich, St. Louis, MO, USA) supplemented with 10% fetal bovine serum (FBS; HyClone, Logan, UT, USA) and 1% penicillin/streptomycin (P/S; Invitrogen, Grand Island, NY, USA). Hereafter, DMEM + 10% FBS + 1% P/S is referred to as DMEM. The collected cells were then filtered through a 70-μm nylon strainer to remove cell aggregates and tissue debris. The filtered BMSCs were cultured in DMEM under standard cell culture conditions (i.e., 37 °C, 5%/95% CO_2/air, humidified, sterile environment) to 90–95% confluency.

The exposure culture method was used to closely mimic the in vivo situation where the pin implant was inserted into bone marrow cavity. Specifically, each sterilized pin sample was placed in a Transwell unit and directly inserted into the established BMSC culture in vitro. That is, the pin samples were cultured in the same wells as BMSCs under this method. Unlike ISO 10993 methods, this exposure culture method permits for studying the effects of degradation products from the samples on the cells directly, without the need for preimmersing the samples in culture media, diluting the media and then applying to the cells. Moreover, the results from this exposure culture could be compared with previous in

vitro studies on ZSr41.[8,9] BMSCs (passage number 1; P1) were detached using trypsin (Invitrogen), seeded in 12-well plates at an initial density of 40 000 cells cm^{-2} in DMEM, and incubated under standard cell culture conditions for an initial period of 1 day. Afterward, the DMEM was removed and replenished with 3 mL of fresh media, and the Transwell inserts (Cat #3460; Corning, Union City, CA) with the sterilized ZSr41 and P–Mg pins at the center were placed into each BMSC-containing well and incubated for 1, 2, and 3 days (D1, D2, D3, respectively). A positive control, designated as "cells" group, consisted of BMSCs cultured in DMEM without any pin samples. DMEM alone was used as a blank reference and designated as "DMEM" group. In order to closely mimic in vivo conditions where the circulation system regularly takes away soluble degradation products from the local site of implantation,[8] the cell culture media was collected for analyses and replenished with 3 mL of fresh media at the same daily intervals.

Fluorescence microscopy was used to evaluate BMSC viability and adhesion on the culture plates at D1, D2, and D3 of culture with ZSr41 and P–Mg pins. At the end of each time point, the Transwell inserts with the ZSr41 and P–Mg pins were removed from the wells and dried in an oven at 37 °C for 2 days. The corresponding wells were washed with a phosphate-buffered saline (PBS) to remove nonadherent cells. Adherent cells on the culture plates, were fixed with 4% formaldehyde (10% neutral buffered formalin; VWR, Radnor, PA, USA) and stained with 4′,6-diamidino-2-phenylindole dilactate (DAPI; Invitrogen) nucleic acid stain and Alexa Flour 488-phalloidin (Life Technologies, Carlsbad, CA) F-actin stain for fluorescence imaging. After staining, the adherent BMSCs on the culture plate were visualized using a fluorescence microscope (Eclipse Ti and NIS software, Nikon, Melville, NY, USA) with a 10× objective lens, and the same exposure condition was used to capture the fluorescence images. These images were then analyzed using ImageJ software (NIH, Bethesda, MD, USA). At least 9 images per well were acquired according to the bulls-eye template and detailed guidelines in the reference[9] to determine BMSC adhesion and viability at 3 different proximities to the samples or degradation products. Specifically, 1 image was taken at the center of each well (designated as R_0), 4 images were taken concentrically at 3.5 mm away from the center of each well (designated as R_1), and 4 images were taken concentrically at 7.0 mm away from the center of each well (designated as R_2). The three regions of R_0, R_1, and R_2 in the tissue culture plates around the Mg-based implants were examined separately to account for the concentration gradient of OH^-, Mg^{2+} ions and other degradation products around each implant. The degradation of Mg-based implants is a dynamic process that continuously releases OH^- and Mg^{2+} ions into the surrounding fluid. That is, R_0 region could have a higher alkalinity and ion concentrations than the R_1 and R_2 regions, thus having different impact on cell adhesion and growth. Cell adhesion density for each group/location/time was quantified by counting the DAPI-stained cell nuclei in each image and calculating the cell density as the number of adherent cells per unit area.

The in vitro degradation of the ZSr41 and P–Mg pins at each time point was evaluated through measurements of sample mass, and pH, and ionic concentrations of the collected media, as well as surface analysis of the samples via SEM, EDS, and XRD. The mass of the dried pins at each time point was measured (M_f) and used to determine a percent final mass relative to the initial mass (i.e., $M_f/M_0 \times 100$; %). The pH of the media was measured immediately after collection using a calibrated pH meter (Model SB70P, VWR). The

concentration of Mg^{2+}, Zn^{2+}, and Sr^{2+} ions in the collected media was measured using inductively coupled plasma optical emission spectrometry (ICP-OES; Optima 8000, PerkinElmer, Waltham, MA, USA). To minimize the matrix effects in ICP-OES, the collected DMEM aliquots were diluted to 1:100 solutions in DI water. Ionic concentrations were then obtained from calibration curves generated using Mg, Zn, and Sr standards (PerkinElmer) diluted to ranges of 0.5–5.0, 0.1–1.0, and 0.1–1.0 mg/L, respectively. Surface topography and elemental composition of the ZSr41 and P–Mg pins after 3 days of culture were characterized using SEM and EDS, respectively. Crystal structures of the phases present on the pin samples after 3 days of culture were analyzed using XRD. Experimental settings for SEM, EDS, and XRD were the same as described in section 2.2. XRD phases were identified according to patterns in the ICSD: 00–004–0770 for Mg, 01–074–6807 for $Mg_{17}Sr_2$, 00–002–0968 for $Ca(OH)_2$, 01–078–4605 for ZnO, 00–002–1395 for $MgO \cdot H_2O$, 00–035–0134 for $Mg_3(PO_4)_2$, 00–053–1189 for $Mg_7(PO_4)_2(OH)_8$, 01–074–6549 for $Ca(HPO_4)(H_2O)_2$, 01–086–0740 for $Ca_5(PO_4)_3(OH)$ (i.e., hydroxyapatite or HA), 00–003–0237 for $Ca_2P_2O_7 \cdot 5H_2O$.

2.5. Degradation of ZSr41 Alloy and Mg Intramedullary Pins and Associated Biological Responses in Vivo

2.5.1. Animal Model and Surgical Procedures—The in vivo degradation and bioactivity of ZSr41 pins and Mg control were evaluated through intramedullary implantation in the proximal tibia of rats for a period of 47 days. The experimental protocol was reviewed and approved by the Institutional Animal Care and Use Committees (IACUC) at the Loma Linda University and the University of California at Riverside (UCR). Eighteen 12-week-old Sprague–Dawley rats were randomly assigned to three groups ($n = 6$ per group). All rats were generally anesthetized in an induction chamber (2% isoflurane in O_2 at 1.5 L/min). Subsequently, the animals were transferred to the operation table, an anesthesia nose cone was placed (1.5% isoflurane in O_2 at 1.5 L/min), and the right stifle (equivalent of the human knee) was shaved with a razor and scrubbed with clorhexadine in preparation for surgery. A longitudinal peripatellar skin incision was made on the medial side of the right leg followed by direct dissection down to the tibial plateau. A drill bit (1/64 in. diameter) was used to prepare predrilled bone tunnels (15 mm in length) in the medullary canal.[35] For two experimental groups, either ZSr41 or P–Mg pins were implanted into predrilled bone tunnels along the axis of the shaft from the proximal tibia using the surgical procedures based on established models.[36–38] In the control group (Sham), the predrilled tunnel was left empty for comparison. The wounds were then carefully sutured with Monochryl 4–0, and the rats were housed in an environmentally controlled animal care laboratory after surgery. Buprenorphine (60 μg/kg) was administered intramuscularly for 2 days as an analgesic. During the surgical procedure, the predrilled canal in one animal for both ZSr41 and P–Mg groups was drilled diagonally through the cortical bone of the mid-diaphysis; therefore, the implanted pins were partially in the medullary canal and partially protruded from the diaphysis. These two animals were observed but not used for qualitative analysis. Table 1 indicates the sample sizes and measurements/data obtained from each animal. Postoperatively, the animals were allowed to move freely in their cages without external support and unrestricted weight bearing, and were fed regularly. The animals were monitored daily to ensure no signs of compromised health, significant inflammation or pain.

Finally, the animals were euthanized by CO_2 inhalation followed by cervical dislocation at 47 days of postsurgery.

2.5.2. Monitoring the Degradation of Intramedullary Pins and Peri-implant Bone in Situ and Ion Concentrations in Blood—Microcomputed tomography (MicroCT or μCT) was used to monitor the pin implants and peri-implant bone tissue in situ. In situ μCT is a nondestructive technique for monitoring the volume change of Mg-based implants as well as peri-implant bone structures surrounding the implant.[27,39–41] As the μCT instruments have been improved over time, we were able to monitor Mg implant degradation in situ, and obtain quantitative measurements of implant degradation and associated bone remodeling, while minimizing the amount of animals needed. The same animal was anesthetized at distinct time points and examined by μCT in this study. Specifically, a μCT setup (MicroCAT II; Imtek Corp., Oak Ridge, TN USA; 74 kVp, 1 mA, 2 s) with a mean voxel size of $63 \times 63 \times 80$ μm^3 was used to visualize proximal tibiae of anesthetized rats at the 3, 7, 12, 28, 39, and 47 days of postsurgery in vivo. A total of 512 transverse two-dimensional (2D) images (512×512 pixels) were acquired over the length of pin implant in the tibia for each anesthetized animal at each time point. Blood was drawn at the days of 0 (immediately after surgery on the day of implantation), 3, 5, 7, 14, 21, 28, 35, and 42 to analyze the concentrations of Mg^{2+}, Zn^{2+}, and Sr^{2+} ions in the blood using the ICP-OES following the same method as described previously in section 2.4.

2.5.3. Quantification of Peri-implant Bone Remodeling and Intramedullary Pin Degradation in Vivo—The in situ μCT measurements provided a reliable method to quantify bone structure, density, and volumes,[39–44] and the in vivo degradation of Mg-based implants in a continuous manner.[27] Peri-implant bone remodeling and implant degradation were visualized and quantified using scale-corrected three-dimensional (3D) digital reconstructions of 2D μCT scans. The 3D structures of implants and peri-implant tissue were reconstructed in IMARIS (Bitplane AG, Zurich, Switzerland) using the volume of interest (VOI) technique with an optimized intensity-based grayscale distribution threshold to isolate tissue (muscle and trabecular and cortical bone) or implants from the background.[45,46] VOIs included ZSr41 and P–Mg implants (along the entire length of the implant), and peri-implant muscle, trabecular bone, and cortical bone regions in the proximal tibia (delimited by the tibial tuberosity and 12.82 ± 50 mm distally from tibial plateau). The volume and mean voxel grayscale intensity of each of the 3D reconstructed VOIs were quantified at the days of 12, 28, and 47 using the volume and mean intensity functions in IMARIS, respectively; additionally, the volume of the ZSr41 and P–Mg pins, and the predrilled cavity of sham were quantified at the days of 0, 3, 7, 12, 28, 39, and 47. The volume of the pins at each time point (V_i) was used to determine a percent final volume relative to the initial volume ($V_i/V_0 \times 100$; %).

Values for the weight density (g cm^{-3}) of each VOI were calculated from mean voxel grayscale intensity; note that the weight density of VOI is not the same as bone mineral density (BMD) for trabecular or compact bone. A calibration curve that converted the mean voxel intensity values of each VOI from μCT to weight density was constructed[47] based on the measured mean voxel intensity ($36,902.1 \pm 217.6$ and $35,582.8 \pm 56.6$ A.U.) and

theoretical weight density (1.90 and 1.74 g cm^{-3}) for the ZSr41 and P–Mg pins, respectively. To calculate the weight density of P–Mg, we used hexagonally close packed configuration for Mg; 2 atoms/unit cell; volume of $1.406a^3$, where $a = 3.210$ Å; and atomic mass of 24.305 g mol^{-1}. The same values were used to calculate the weight density of ZSr41, with the exception that the atomic mass was 26.581 g mol^{-1} for 95 wt % Mg, 4 wt % Zn, and 1 wt % Sr.

2.5.4. Surface Characterization of Dissected Pin Implants—Surface topography and elemental composition of the ZSr41 and P–Mg intramedullary pins after implantation in rat tibiae for 47 days were characterized using SEM and EDS, respectively. Additionally, elemental distribution maps on the surface of dissected pins were obtained for Mg, Ca, and P (Ka lines). Crystal structures of the phases present were analyzed with XRD. Experimental settings for SEM, EDS, and XRD were the same as outlined in section 2.2. The right tibia from one sham specimen was dissected, lyophilized overnight, and pulverized with a mortar and pestle for XRD analysis (reference spectrum for bone). XRD phases were identified according to patterns in the ICSD: 00-004-0770 for Mg, 03-065-3649 for $Mg_{17}Sr_2$, 00-044-1482 for $Mg(OH)_2$, 01-084-1272 for $Ca(OH)_2$, 01-079-8260 for $Mg_3(PO_4)_2$, and 00-001-1008 for $Ca_{10}(PO_4)_6(OH)_2$ (i.e., hydroxyapatite or HA).

2.5.5. Elemental Mapping Analysis at the Implant-Tissue Interface—Elemental mapping analysis was used to study the elemental compositions at the implant-tissue interface, the release and diffusion of alloying elements into peri-implant bone tissue, and peri-implant bone remodeling in response to the degradation of the ZSr41 and P–Mg intramedullary pins. For elemental mapping analysis, one complete right tibia from each group was harvested, and then the muscle and periosteum was dissected. Subsequently, the complete tibia was lyophilized overnight, and embedded in a low viscosity epoxy resin (catalog no. ULTRA-3000R-32, Pace Technologies, Tucson, AZ, USA) in vacuum. The embedded complete tibia was sectioned transversely at the mid-diaphysis 5 mm from the tibia plateau using a low speed saw (Model 650; South Bay Technology, Inc., San Clemente, CA, USA) equipped with a diamond wheel (0.305 mm thick, catalog no. DWH4122; South Bay Technology, Inc.) to obtain calcified transverse sections. Subsequently, the sections were sputter coated (Model 108, Cressington Scientific Instruments Ltd., Watford, UK) with platinum/palladium at 20 mA for 40 s of sputter time. Surface microstructure and elemental distribution maps for Mg, Zn, Sr, Ca, and P (Ka lines) were characterized using SEM and EDS, respectively. EDS point analyses were utilized to semiquantitatively investigate the atomic ratio of Ca/P (i.e., atomic percent of Ca divided by atomic percent of P) in the peri-implant cortical bone regions and in the newly formed bone fractions as a measure of bone quality.

2.5.6. Histological Evaluations Postsurgery—Plastic-embedded calcified sections were used for histological evaluations of the sites with ZSr41 and P–Mg intramedullary pin implants and sham at the 47 days of postsurgery. Post-mortem histology imaging provides complementary information for in situ μCT imaging. Two complete right tibiae from each group were harvested and fixed in 10% neutral buffered formalin for 24 h for histological evaluations. After serial dehydration in the solutions with increasing ethanol concentrations

$(2 \times 70\%, 2 \times 95\%, 2 \times 100\%; 3 \text{ h each})$, the harvested tibiae were embedded in methyl methacrylate (MMA). Specific details regarding infiltration and embedding solutions, and embedding process were described elsewhere.[48] The resin blocks were cut into thick sections (~200 μm thick) using a diamond-embedded wire saw (Model 3241; Well Diamond Wire Saws Inc., Norcross, GA USA). The thick sections were re-embedded in MMA and cut into serial 5–10 μm proximal sagittal sections or transverse thin sections (at mid-diaphysis 6 mm from tibial plateau) using a rotary microtome (Model 5030; Bright Instruments Ltd., Cambridgeshire, UK) equipped with a D-profile tungsten carbide blade (Delaware Diamond Knives, Inc., Wilmington, DE USA). All these sections were undecalcified. Serial thin sections were stained with Goldner's trichrome stain for analysis of bone structure[49] and with toluidine blue (0.1% toluidine blue O in 0.1% borax solution for 10 s) for analysis of cell and cartilage distribution. The stained sections were observed and imaged using an optical microscope.

2.6. Analyzing the Degradation Rates of ZSr41 Alloy and Mg Intramedullary Pins in Vitro and in Vivo

ZSr41 and P–Mg pin volume (V_i) from 3D reconstruction analyses at distinct time points was used to establish a model for the degradation of Mg-based intramedullary pins in the rat tibia. To capture the differences in pin volume, the volume of each pin at each time point (V_i) was normalized by its corresponding initial volume (V_0). A linear model with the y-intercept set to unity was used to fit the ratio of V_i/V_0 as a function of time in weeks; the model was used to predict the lifetimes of the ZSr41 and P–Mg intramedullary pins in vivo.

In vitro average daily degradation rates (i.e., ion release rates) for the ZSr41 and P–Mg pins were calculated based on the measured Mg^{2+} ion concentrations in the BMSC/DMEM culture system. The in vitro degradation rates, either normalized by initial volume (V_0) or by initial surface area (SA_0) of the pin sample, were calculated according to the following equations (eqs 1a and 1b, respectively):

$$\frac{\text{avg. daily deg. rate}}{\text{unit initil vol.}} = \frac{[\sum_{i=1}^{3}([Mg^{2+}]_i) - [Mg^{2+}]_{DMEM,tot}] \times 0.003\,L}{3\,\text{day} \times V_0} \quad (1a)$$

$$\frac{\text{avg. daily deg. rate}}{\text{unit initial surf. area}} = \frac{[\sum_{i=1}^{3}([g^{2+}]_i) - [Mg^{2+}]_{DMEM,tot}] \times 0.003\,L}{3\,\text{day} \times SA_0} \quad (1b)$$

The data from the 3-day in vitro culture with BMSCs were used in the calculations with eq 1a to represent the three distinct time points (1, 2, 3 days). Furthermore, eq 1a was first used to calculate the average daily degradation rate for each pin replicate in each group and then the mean value for each group (ZSr41, P–Mg) was calculated. In eq 1a, $[Mg^{2+}]$ were measured originally in mg/L using ICP-OES. The total measured concentration in blank DMEM over the 3 day period, $[Mg^{2+}]_{DMEM,tot}$, was 55.8 mg/L. The measured $[Mg^{2+}]_{DMEM}$ per day was 0.765 mM, which was very close to the nominal value of 0.8 mM.[50] That is,

$[Mg^{2+}]_{DMEM,tot}$ = 0.765 mmol L^{-1} × 24.305 mg $mmol^{-1}$ × 3 = 55.8 mg/L. The immersion media volume was 3 mL (0.003 L); the average daily rate was computed from a 3-day period; and the computed rate (mg day^{-1}) was normalized by either V_0 (cm^3) or SA_0 (cm^2) of each pin replicate.

In vivo average daily degradation rates (i.e., volume loss rates) for the ZSr41 and P–Mg pins were calculated based on the volume change from 3D reconstructions of μCT images. The in vivo degradation rates, either normalized by initial volume (V_0) or by initial surface area (SA_0) of each pin implant, were calculated according to the following equations (eqs 2a and 2b, respectively):

$$\frac{\text{avg. daily deg. rate}}{\text{unit initial vol.}} = \frac{(V_0 - V_{47}) \times \rho}{47\,\text{day} \times V_0} \quad \text{(2a)}$$

$$\frac{\text{avg. daily deg. rate}}{\text{unit initial surf. area}} = \frac{(V_0 - V_{47}) \times \rho}{47\,\text{day} \times SA_0} \quad \text{(2b)}$$

The volume values of pin implants at day 47 (V_{47}) were used to calculate the average daily degradation rates. Eq 2a was first used to calculate the average daily degradation rate for each pin implant in each group and then the mean value for each group (ZSr41, P–Mg) was calculated. Volume values (cm^3) of pins were obtained from the 3D reconstructed μCT images using the Volume function in IMARIS. The weight density of each pin was either $\rho_{ZSr41} = 1.90 \times 10^3$ mg cm^{-3} or $\rho_{P-Mg} = 1.74 \times 10^3$ mg cm^{-3}; the average daily degradation rate was computed from a 47-day period, and the computed rate (mg day^{-1}) was normalized by either V_0 (cm^3) or SA_0 (cm^2) of each pin implant.

Additionally, the in vitro and in vivo average daily degradation rates per unit area for ZSr41 and P–Mg pins from this study were compared with the in vitro degradation rates from the following studies on ZSr41 alloys: ZSr41 and P–Mg sheets in the exposure culture (i.e., samples were placed in Transwell inserts in the culture well) with H9 human embryonic stem cells (H9-hESCs) in mTeSR media (average from 3 days);[8] ZSr41 and P–Mg sheets in the direct culture (i.e., cells were seeded directly onto sample surface) with human umbilical vein endothelial cells (HUVECs) in EGM-2 media (average from 1 day)[10] ZSr41 and P–Mg sheets in the direct culture with BMSCs in DMEM media (average from 3 days).[11]

2.7. Statistical Analyses

Electrochemical, cytocompatibility, and in vitro degradation experiments were run in triplicate. Sample sizes for in vivo measurements are outlined in Table 1. All data sets were tested for normal distribution and homogeneous variance. Parametric data sets were analyzed using one-way analysis of variance (ANOVA) followed by the Tukey HSD post hoc test. Data sets with normal distribution but heterogeneous variance were analyzed using one-way ANOVA (homogeneous variance not assumed) followed by the Games-Howell post hoc test. Nonparametric data sets were analyzed using the Kruskal–Wallis test followed by

either the Nemenyi post hoc test (equal sample sizes) or the Dunn post hoc test (unequal sample sizes). Statistical significance was considered at $p < 0.05$.

3. RESULTS

3.1. Surface Characterization of ZSr41 Alloy and Mg Pins

Figure 1 summarizes the results for surface characterization of polished, and autoclaved ZSr41 and P–Mg pins. The SEM images (1000×) in Figure 1a and 1b show the polished surfaces of the ZSr41 and P–Mg pins, respectively. Based on our previous metallographic characterization, the ZSr41 alloy showed Mg as a matrix phase, and Zn and Sr predominantly existed in the form of precipitates at the grain boundaries as secondary β-phases.[7] The micrographs in Figure 1a and 1b confirmed the presence of a network of secondary β-phase (white web-like structures) on the ZSr41 pin but not on P–Mg. EDS surface elemental composition analysis (Figure 1a and 1b, insets, tables) confirmed the presence of Zn and Sr on the ZSr41 pin but not on P–Mg. Specifically, the ZSr41 pin had 4.0 wt % Zn and 0.9 wt % Sr in a Mg matrix, along with residual surface oxides (1.1 wt %); in contrast, P–Mg only had residual oxides (1.5 wt %) in a Mg matrix. XRD results confirmed crystalline Mg, $(Mg_{0.25}Zn_{0.75})O$, $Mg_{17}Sr_2$, Mg_7Zn_3 (Figure 1a$'$) on the polished surface of ZSr41, and crystalline Mg, $Mg(OH)_2$, and MgO (Figure 1b$'$) on the polished surface of P–Mg. The SEM images (160×) in Figure 1c and 1d show the autoclaved surfaces of the ZSr41 and P–Mg pins, respectively; and, the nucleation of micron-scale oxide structures was observed predominantly on the surface of the ZSr41 pin and to a much lower extent on P–Mg. Additional SEM images (Figure 1c and 1d, insets; 500×) of a side-view at the periphery of the ZSr41 and P–Mg pins, respectively, show that the oxide structures on the ZSr41 pin self-assembled to a height of 35 μm. EDS surface elemental composition analyses of the samples after autoclaving (Figure 1c and 1d, insets, tables) confirmed an oxide-enriched surface for ZSr41, and to a lower extent for P–Mg. Specifically, the oxygen content on the surface of ZSr41 increased to 36.6 wt % after autoclaving; meanwhile, the Zn and Sr content remained in close proximity to the nominal value. In contrast, the oxygen content on the surface of P–Mg pin was 18.2 wt % after autoclaving. XRD results after autoclaving confirmed crystalline Mg, $Mg(OH)_2$, SrO, and $Mg_{17}Sr_2$, Mg_7Zn_3 (Figure 1c$'$) and crystalline Mg, $Mg(OH)_2$, and MgO (Figure 1d$'$) on the polished and then autoclaved surfaces of ZSr41 and P–Mg, respectively.

3.2. Corrosion Properties of ZSr41 Alloy and Mg Pins from Electrochemical Testing

PDP curves obtained for the as-polished pin samples showed that the initial corrosion (or degradation) behavior of the ZSr41 and P–Mg pins was similar (Figure 2). The median PDP trace with the most representative corrosion potential (E_{corr}) and corrosion current density (J_{corr}) for each sample type was plotted in Figure 2a. A qualitative assessment of the PDP curves indicated that the as-polished ZSr41 sample was slightly more cathodic when compared to P–Mg. Furthermore, assessment of the linear anodic (b_a) and cathodic (b_c) portions of the PDP curves gave indication that ZSr41 and P–Mg had similar half-reaction characteristics. ANOVA was used to confirm statistically significant differences in the E_{corr} [F (1, 4) = 9.4064, $p = 3.74 \times 10^{-2}$] values calculated by Tafel extrapolation from the PDP curves (Figure 2b). Post hoc pairwise comparisons confirmed that the E_{corr} of ZSr41 (−1.60

± 0.03 V; mean ± SD) was significantly more cathodic ($p < 0.05$) when compared with P–Mg (−1.66 ± 0.01 V). Significant differences in J_{corr} values calculated by Tafel extrapolation (Figure 2c) were not detected between the mean value for ZSr41 (33.77 ± 3.60 mA cm^{-2}; mean ± SD) and P–Mg (45.40 ± 8.23 mA cm^{-2}).

3.3. Cytocompatibility of ZSr41 Alloy and Mg Pins in Exposure Culture with Bmscs in Vitro

Cytocompatibility of ZSr41 and P–Mg pins with BMSCs was evaluated through cell adhesion density on the culture plates in a 3-day period, and the results are summarized in Figure 3a–3d. Figure 3a shows representative fluorescence images of BMSCs attached to the culture plates at R_1 location during D1, D2, and D3 postincubation; similarly, images were obtained at R_0 and R_2 locations during the same incubation intervals. The DAPI-stained nuclei were used to quantify BMSC adhesion density at the locations R_0, R_1, and R_2 inside each well during each incubation interval, and the results are plotted in Figure 3b–3d, for each respective location. ANOVA was used to confirm statistically significant differences for BMSC adhesion density at the location R_1 at D3 [F (2, 6) = 14.179, $p = 5.33 \times 10^{-3}$]; family-wise comparison of BMSC adhesion densities at all other locations and time points did not yield statistically significant differences. Post hoc pairwise comparisons confirmed that the mean BMSC adhesion density in exposure culture with ZSr41 (22.12 ± 1.37 × 10^3 cells cm^{-2}; mean ± SE) was statistically lower ($p < 0.01$) than the BMSCs-only positive control (29.92 ± 0.79 × 10^3 cells cm^{-2}) only at D3 at location R_1; however, scientifically, this difference was considered trivial because BMSCs reached the state of confluence in both groups. Moreover, statistically significant differences between the ZSr41 group and the BMSCs-only control were not detected at D1, D2, and D3 at the locations R_0 and R_2, and at D1 and D2 at the location R_1; the location R_0 was closer to the samples than location R_1. BMSC adhesion densities in the culture with the ZSr41 pins showed no statistically significant differences when compared with the P–Mg group at all locations R_0, R_1, and R_2 over the 3-day culture period. A comparison between cell adhesion densities at each location for each group showed a general trend of increasing cell densities with increasing incubation time, indicating cell proliferation over time.

3.4. In Vitro Degradation of ZSr41 Alloy and Mg Pins in the BMSC/DMEM Culture System

Results for the in vitro degradation of the ZSr41 and P–Mg pins during 3 days of incubation intervals (D1, D2, and D3) are summarized in Figure 3e–3g. Sample mass change (Figure 3e), media pH (Figure 3f), and Mg^{2+} ion concentration in media ([Mg^{2+}]; Figure 3g) are important indicators for the degradation of Mg-based materials.[26] ANOVA showed statistically significant differences in the mean percent final/initial mass ($M_f/M_0 \times 100$; Figure 3e) of ZSr41 and P–Mg at D2 [F(1, 4) = 10.027, $p = 3.40 \times 10^{-2}$] and D3 [F(1, 4) = 17.126, $p = 1.44 \times 10^{-2}$]; no significant family wise differences were detected at D1. Post hoc pairwise comparisons confirmed a statistically lower final/initial mass percent at D2 ($p < 0.05$) for ZSr41 (97.94 ± 0.71%; mean ± SD) when compared with P–Mg (101.74 ± 1.95%), and at D3 ($p < 0.05$) for ZSr41 (96.62 ± 0.70%) when compared with P–Mg (99.98 ± 1.22%). Similarly, ANOVA (without homogeneous variance) confirmed statistically significant differences in the mean pH of the incubation media at D1 [F (3, 8) = 88.645, $p = 2.72 \times 10^{-6}$], and ANOVA (with homogeneous variance) confirmed differences at D2 [F (3, 17) = 71.028, $p = 8.01 \times 10^{-10}$] and D3 [F (3, 4) = 13.314, $p = 2.37 \times 10^{-2}$] (Figure 3f). Post

hoc pairwise comparisons at D1 confirmed a significantly more alkaline media for ZSr41 (8.19 ± 0.03; mean ± SD) than P–Mg (8.01 ± 0.01; $p < 0.001$), BMSCs-only positive control (7.99 ± 0.01; $p < 0.001$), and DMEM-only blank reference (8.07 ± 0.03; $p < 0.01$); interestingly, the media pH of BMSCs-only group was significantly lower than P–Mg group ($p < 0.001$) and DMEM reference ($p < 0.05$). At D2, post hoc comparisons confirmed a significantly more alkaline media ($p < 0.001$) for ZSr41 (8.10 ± 0.03) than P–Mg (7.97 ± 0.01), BMSCs-only (7.93 ± 0.02), and DMEM-only (7.99 ± 0.01) groups; and the media pH of BMSCs-only group was statistically lower ($p < 0.01$) than DMEM-only reference. At D3, post hoc comparisons confirmed a significantly more alkaline media ($p < 0.05$) for ZSr41 (8.05 ± 0.02) than P–Mg (7.94 ± 0.02), BMSC (7.94 ± 0.03), and DMEM (7.98 ± 0.00) groups. Additionally, the Kruskal–Wallis test for nonparametric data confirmed statistically significant differences in the mean $[Mg^{2+}]$ at D1 [X^2 (3, N = 30) = 26.124, $p = 8.99 \times 10^{-6}$], ANOVA (without homogeneous variance) confirmed significant differences at D2 [F (3, 9) = 278.720, $p = 4.37 \times 10^{-9}$], and ANOVA (with homogeneous variance) confirmed significant differences at D3 [F (3, 8) = 3034.9, $p = 1.46 \times 10^{-12}$] (Figure 3g). Post hoc pairwise comparisons at D1 confirmed a significantly higher $[Mg^{2+}]$ ($p < 0.001$) for ZSr41 (6.92 ± 1.32 mM; mean ± SD) than P–Mg (1.61 ± 0.13 mM), BMSC (0.78 ± 0.01 mM), and DMEM (0.77 ± 0.00 mM) groups. At D2, post hoc comparisons confirmed a significantly higher $[Mg^{2+}]$ ($p < 0.001$) for ZSr41 (6.00 ± 0.45 mM) than P–Mg (1.41 ± 0.14 mM), BMSC (0.70 ± 0.03 mM), and DMEM (0.74 ± 0.01 mM) groups; a significantly higher $[Mg^{2+}]$ ($p < 0.001$) was confirmed for P–Mg than BMSC and DMEM reference groups. At D3, post hoc comparisons confirmed a significantly higher $[Mg^{2+}]$ ($p < 0.001$) for ZSr41 (4.77 ± 0.06 mM) than P–Mg (1.32 ± 0.03 mM), BMSC (0.71 ± 0.10 mM), and DMEM (0.79 ± 0.02 mM) groups; furthermore, a significantly higher $[Mg^{2+}]$ ($p < 0.001$) was confirmed for P–Mg than BMSC and DMEM reference groups.

The Zn^{2+} and Sr^{2+} ion concentrations ($[Zn^{2+}]$ and $[Sr^{2+}]$, respectively) in the culture media were also measured to ensure their concentrations remained below cytotoxic levels reported in literature. P–Mg served as a control group without Zn and Sr alloying elements for the ZSr41 group. BMSC and DMEM were included as the reference groups to show the baseline and deviation of the ion concentrations in the BMSC/DMEM culture system and in the DMEM itself. Results for $[Zn^{2+}]$ and $[Sr^{2+}]$ during D1–D3 incubation intervals are summarized in Figure 3h and 3i, respectively. The Kruskal–Wallis test confirmed statistically significant differences in the mean $[Zn^{2+}]$ at D1 [X^2 (3, N = 30) = 18.503, $p = 3.46 \times 10^{-4}$], at D2 [X^2 (3, N = 21) = 13.355, $p = 3.93 \times 10^{-4}$], and D3 [X^2 (3, N = 12) = 6.590, $p = 8.62 \times 10^{-4}$] (Figure 3h). Post hoc pairwise comparisons at D1 confirmed a significantly higher $[Zn^{2+}]$ ($p < 0.001$) for ZSr41 (39.83 ± 6.65 μM; mean ± SD) than P–Mg (3.03 ± 3.12 μM), BMSC (2.12 ± 0.38 μM), and DMEM (2.06 ± 0.15 μM) groups. At D2, post hoc comparisons confirmed a significantly higher $[Zn^{2+}]$ ($p < 0.001$) for ZSr41 (39.02 ± 4.75 μM) than P–Mg (1.79 ± 0.56 μM), BMSC (1.87 ± 0.35 μM), and DMEM (2.19 ± 0.18 μM) groups. Similarly, at D3 post hoc comparisons confirmed a significantly higher $[Zn^{2+}]$ ($p < 0.001$) for ZSr41 (38.33 ± 2.78 μM) than P–Mg (2.36 ± 0.53 μM), BMSC (2.28 ± 0.57 μM), and DMEM (2.43 ± 0.11 μM) groups. In addition, the Kruskal–Wallis test confirmed statistically significant differences in the mean $[Sr^{2+}]$ at D1 [X^2 (3, N = 30) = 21.077, $p = 1.02 \times 10^{-4}$], while ANOVA (without homogeneous variance) confirmed statistically

significant differences at D2 [F (3, 9) = 60.005, p = 2.24 × 10^{-6}] and at D3 [F (3, 4) = 25.795, p = 6.02 × 10^{-4}] (Figure 3i). Post hoc pairwise comparisons at D1 confirmed a significantly higher [Sr^{2+}] (p < 0.001) for ZSr41 (20.83 ± 5.30 μM; mean ± SD) than P–Mg (1.22 ± 2.31 μM), BMSC (0.22 ± 0.45 μM), and DMEM (0.38 ± 0.66 μM) groups. At D2, *post hoc* comparisons confirmed a significantly higher [Sr^{2+}] (p < 0.001) for ZSr41 (13.95 ± 2.35 μM) than P–Mg (0.24 ± 0.59 μM), BMSC (1.20 ± 1.56 μM), and DMEM (0.12 ± 0.21 μM) groups. Similarly, at D3, post hoc comparisons confirmed a significantly higher [Sr^{2+}] (p < 0.001) for ZSr41 (16.43 ± 2.81 μM) than P–Mg (1.12 ± 0.64 μM), BMSC (0.13 ± 0.23 μM), and DMEM (0.51 ± 0.88 μM) groups.

Figure 4 summarizes the results for surface characterization of ZSr41 and P–Mg pins after 3 days of culture with BMSCs in DMEM. The SEM images (65×) in Figure 1a and 1b were obtained from the center (lengthwise) of the pins and show the corroded surfaces of the ZSr41 and P–Mg, respectively. At the center of the pins (Figure 4a and 4b), the surface of ZSr41 showed more deposition of degradation products and more homogeneous distribution of degradation products than that on P–Mg. Similarly, at the end of the pins (Figure 4a and 4b, insets), ZSr41 showed more deposition and more homogeneous degradation products on the surface than P–Mg. After immersion in DMEM, XRD results confirmed crystalline phases of Mg, Ca(OH)$_2$, ZnO, MgO·H$_2$O, Ca(HPO$_4$)(H$_2$O)$_2$, and Ca$_5$(PO$_4$)$_3$(OH) (i.e., hydroxyapatite or HA), Mg$_{17}$Sr$_2$ (Figure 4a′) on the corroded surfaces of ZSr41, and crystalline phases of Mg, Ca(OH)$_2$, Mg$_3$(PO$_4$)$_2$, Mg$_7$(PO$_4$)$_2$(OH)$_8$, Ca$_2$P$_2$O$_7$·5H$_2$O (Figure 4b′) on the corroded surfaces of P–Mg. The peaks of calcium phases in Figure 4a′ and 4b′ were small, but they were detected in the HighScore software and visible in a magnified view. EDS analysis (Figure 4c) confirmed the presence of Zn and Sr on the ZSr41 pin but not on P–Mg, a higher oxide content on ZSr41 than on P–Mg. Specifically, the ZSr41 pin showed (in atomic %) 71.2% O, 20.1% Mg, 0.4% Zn, 0.1% Sr, 3.5% Ca, 2.7% P, and 2.1% Na, Cl, and K; the P–Mg had 61.1% O, 30.0% Mg, 2.5% Ca, 5.7% P, and 0.8% Na, Cl, and K. Based on these values, the Ca/P atomic ratio on ZSr41 and P–Mg was 1.31 and 0.44, respectively.

3.5. In Vivo Degradation of ZSr41 Alloy and Mg Intramedullary Pins and Peri-implant Bone Remodeling

Figure 5 summarizes the results of in vivo degradation of ZSr41 and P–Mg intramedullary pins over an implantation period of 47 days in rat tibiae. Figure 5a shows representative in vivo μCT images from the mid-diaphysis of the proximal tibia at a 5 mm distance from the tibial plateau for all groups at the selected time points throughout the 47-day study. The same animal scanned at the same location of proximal tibia at each time point was used for each group. The μCT images confirmed gradual degradation of ZSr41 and P–Mg intra-medullary pins in vivo, and extensive peri-implant cortical bone formation in response to the degradation of ZSr41 and P–Mg pins starting from D12 throughout D47. Qualitatively, the growth of new bone around ZSr41 pins seemed to be more than that around P–Mg pins. The μCT images also showed the presence of peri-implant gas pockets (dark spots) for both ZSr41 and P–Mg groups throughout D47. Interestingly, the distribution of gas pockets appeared quite different for ZSr41 versus P–Mg groups. For ZSr41 group, the gas pockets seemed to be less and smaller in the bone tunnel around the ZSr41 pins with more gas

pockets spreading to the cortical bone region. In contrast, for P–Mg group, more and larger gas pockets appeared inside the bone tunnel around the P–Mg pins with very little spreading into the cortical bone region.

The respective Mg^{2+}, Zn^{2+}, and Sr^{2+} ion concentrations in the collected rat blood during the implantation period of ZSr41 and P–Mg intramedullary pins are plotted in Figure 5b–5d. P–Mg served as a control group without Zn and Sr alloying elements, while the sham group was included as the reference to show the baseline and deviation of the ion concentrations in the rat blood. The results of statistical analyses on measured ionic concentrations in the rat blood, including the concentration values (mean ± SD) and statistically significant differences, are summarized in Table 2. Even though several statistically significant differences were detected during D0–D28, these differences were not biologically meaningful because either the ionic concentrations in the Sham group were higher than the ZSr41 and P–Mg groups or the difference was smaller than the random biological variations. At D35 and D42, no statistically significant differences were detected for any of the ions measured for any of the groups. Clearly, ZSr41 and P–Mg intramedullary pins did not induce systemic change in Mg^{2+}, Zn^{2+}, and Sr^{2+} ionic concentrations in rat blood throughout this in vivo study; all the changes were within the random biological variations.

Figure 6 summarizes the 3D reconstructed VOIs, quantification of peri-implant bone remodeling and implant volume change over the 47-day implantation period of ZSr41 and P–Mg intramedullary pins. Figure 6a shows representative images of 3D reconstructions of the proximal tibia with ZSr41 or P–Mg implants at D12, D28, and D47 postimplantation in comparison with the Sham control. The μCT images from the same animal within each group at the respective time points were used to directly compare sequential bone remodeling. The reconstructed 3D images confirmed extensive bone remodeling and growth, and formation of gas pockets in the proximal tibia in the ZSr41 and P–Mg groups, in contrast to the Sham control. Visually, the 3D images showed that the peri-implant proximal tibia for ZSr41 and P–Mg pins increased in volume over time; the ZSr41 group seemed to have a greater bone volume and more gas-induced cavities than P–Mg group. Further, the peri-implant bone volume (trabecular and cortical) were quantified for the representative time points of D12, 28, and D47, and plotted in Figure 6b–6d, respectively. At D12 (Figure 6b), although the average volume of cortical bone was higher in the ZSr41 group and the average volume of trabecular bone was lower in the ZSr41 group when compared with the P–Mg group and Sham control, no statistical significance was detected. At D28 (Figure 6c), ANOVA confirmed statistically significant differences in the mean cortical bone volume [$F_{(2, 13)} = 5.797$, $p = 1.59 \times 10^{-2}$], but the difference in the mean trabecular bone volume remained statistically undetectable for all groups. Specifically, post hoc pairwise comparisons showed that the peri-implant cortical bone volume for ZSr41 ($1.07 \pm 0.14 \times 10^2$ mm^3; mean ± SD) was significantly higher ($p < 0.05$) than the Sham control ($0.83 \pm 0.05 \times 10^2$ mm^3). Interestingly, the average volume of cortical bone and the average volume of trabecular bone in the ZSr41 group were greater than that of P–Mg group, and the average bone volumes in the P–Mg group were greater than that of the Sham control, but not statistically significant at D28. At D47 (Figure 6d), ANOVA confirmed statistical differences in the volumes of peri-implant trabecular bone [$F_{(2, 11)} = 4.634$, $p = 3.47 \times 10^{-2}$] and cortical bone [$F_{(2, 11)} = 63.486$, $p = 9.10 \times 10^{-7}$]. Post hoc pairwise comparisons of bone

volumes confirmed a significantly higher trabecular bone volume ($p < 0.05$) for the ZSr41 group ($1.49 \pm 0.34 \times 10^2$ mm^3) than the Sham control ($0.84 \pm 0.19 \times 10^2$ mm^3), and a significantly higher cortical bone volume ($p < 0.001$) for the ZSr41 group ($1.71 \pm 0.20 \times 10^2$ mm^3) than the P–Mg group ($0.90 \pm 0.10 \times 10^2$ mm^3) and the Sham control ($0.77 \pm 0.10 \times 10^2$ mm^3) at D47. Even though the average bone volumes in the P–Mg group were greater than that of the Sham control, but still not statistically significant at D47.

Figure 6e–6g summarizes the quantification of the weight density for peri-implant muscle, trabecular bone, cortical bone, and that of the ZSr41 and P–Mg implants at D12, D28, and D47 postimplantation. At D12 (Figure 6e), ANOVA confirmed statistically significant differences only for the weight density of trabecular bone region [$F_{(2, 9)} = 10.14$, $p = 4.95 \times 10^{-3}$] and post hoc pairwise comparisons showed that the weight density of trabecular bone in the ZSr41 (1.67 ± 0.02 g cm^{-3}) group was significantly greater ($p < 0.01$) than that of the P–Mg (1.60 ± 0.03 g cm^{-3}; mean $\pm$ SD) group; and that of the P–Mg group was significantly lower than the Sham control (1.66 ± 0.02 g cm^{-3}). At D28 (Figure 6f), the Kruskal–Wallis test confirmed statistically significant differences in the mean weight density of trabecular bone region [$X2(2, N = 16) = 10.488$, $p = 5.28 \times 10^{-3}$] and ANOVA (without homogeneous variance) confirmed significant differences in the mean weight density of the cortical bone region [$F_{(2, 6)} = 8.622$, $p = 1.64 \times 10^{-2}$]. Specifically, post hoc pairwise comparisons showed that the weight density of the peri-implant trabecular bone around P–Mg group (1.58 ± 0.02 g cm^{-3}) was significantly lower ($p < 0.01$) than the Sham control (1.65 ± 0.01 g cm^{-3}), and the weight density of the peri-implant cortical bone around the ZSr41 group (1.81 ± 0.03 g cm^{-3}) was significantly lower than the P–Mg group (1.85 ± 0.02 g cm^{-3}; $p < 0.05$) and the Sham control (1.87 ± 0.01 g cm^{-3}; $p < 0.01$). At D47 (Figure 6g), ANOVA confirmed statistically significant differences only for the weight density of cortical bone region [$F_{(2, 11)} = 12.304$, $p = 1.56 \times 10^{-3}$] and *post hoc* pairwise comparisons showed that the weight density of cortical bone in the ZSr41 group (1.80 ± 0.04 g cm^{-3}) was significantly lower ($p < 0.01$) than the P–Mg group (1.86 ± 0.01 g cm^{-3}) and the Sham control (1.88 ± 0.02 g cm^{-3}). In all cases, the weight density of the peri-implant muscle region was always 1.55–1.56 g cm^{-3}; and the weight density of the cortical bone in the Sham control was always 1.86–1.88 g cm^{-3} at all the time points, which is in close agreement with published values of 1.80–1.92 g cm^{-3} in literature.[51] As expected, the weight density of the ZSr41 pins was always greater than the P–Mg pins at all the time points; and their respective weight density was in close agreement with the theoretical values for the ZSr41 and P–Mg pins (1.90 and 1.74 g cm^{-3}, respectively). The weight density of ZSr41 pin decreased over time from 1.91 g cm^{-3} at D12, 1.90 g cm^{-3} at D28, and 1.89 g cm^{-3} at D47, while the weight density of P–Mg pin remained the same at 1.74 g cm^{-3}.

Figure 6h shows the representative 3D images of ZSr41 and P–Mg intramedullary pins reconstructed from the in situ μCT scans of the proximal rat tibia over the 47-day implantation period. To directly compare the sequential implant degradation in situ, the same implant in the same animal within each group was used for the 3D image reconstruction. For the ZSr41 group, a portion of image was missing at D7 because of a misalignment of the μCT scan and the missing portion is indicated with the dashed line in Figure 6h. Qualitatively, the ZSr41 intramedullary pins showed homogeneous degradation initially (i.e., bulk corrosion from all sides) until D28; and thereafter, the ZSr41 implants lost structural

integrity and degraded into smaller segments. In contrast, P–Mg pins started with homogeneous degradation until D12, and then significant thinning around the center of the pin stated at D28; P–Mg pins maintained structural continuity without apparent fragmentation over the 47-day implantation period. In general, the ZSr41 pins showed a faster degradation rate than P–Mg in vivo. Quantitatively, the volume changes of the pin implants (V_i/V_0), that is, the percent volume of the implants at each time point (V_i) relative to their paired initial volume (V_0), are plotted in Figure 6i. The Sham control in Figure 6i shows the volume change of the predrilled cavity in rat tibiae because no implants were inserted, that is, volume reduction of the bone tunnel as a result of filling of newly formed bone. Statistical comparisons for the following data points were not included in Figure 6i: ZSr41 and P–Mg at D3 ($n_{D3,ZSr41} = 2$ and $n_{D3,P-Mg} = 2$), ZSr41 at D7 ($n_{D7,ZSr41} = 1$), and Sham at D39 ($n_{D39,Sham} = 0$) because of the absence of replicate data (see Table 1). ANOVA confirmed significant differences in the mean percent volume at D7 [$F(1, 6) = 693.66$, $p = 1.98 \times 10^{-7}$], D12 [$F(2, 9) = 60.53$, $p = 6.03 \times 10^{-6}$], D28 [$F(2, 15) = 203.94$, $p = 1.33 \times 10^{-11}$], D39 [$F(1, 8) = 102.70$, $p = 7.69 \times 10^{-6}$], and D47 (without homogeneous variance) [$F(2, 8) = 182.911$, $p = 3.91 \times 10^{-7}$]. Post hoc pairwise comparisons showed the following significant differences in the percent volume: at D7, Sham ($17.96 \pm 4.36\%$) was significantly lower ($p < 0.001$) than P–Mg ($89.03 \pm 3.18\%$); at D12, Sham ($11.44 \pm 3.43\%$) was significantly lower ($p < 0.001$) than ZSr41 ($59.25 \pm 13.89\%$) and P–Mg ($80.38 \pm 6.52\%$), and ZSr41 was significantly lower ($p < 0.05$) than P–Mg; at D28, Sham ($8.35 \pm 3.45\%$) was significantly lower ($p < 0.001$) than ZSr41 ($36.05 \pm 5.58\%$) and P–Mg ($70.85 \pm 6.60\%$), and ZSr41 was significantly lower ($p < 0.001$) than P–Mg; at D39, ZSr41 ($29.43 \pm 6.11\%$) was significantly lower ($p < 0.001$) than P–Mg ($61.14 \pm 3.41\%$); and at D47, Sham ($3.18 \pm 1.81\%$) was significantly lower than ZSr41 ($13.01 \pm 6.58\%$; $p < 0.05$) and P–Mg ($58.10 \pm 6.53\%$; $p < 0.001$), and ZSr41 was significantly lower ($p < 0.001$) than P–Mg. Overall, the volume reduction rate of ZSr41 pins was faster than that of P–Mg over the 47-day implantation period; and the volume reduction rate of the ZSr41 pins more closely matched the volume reduction rate of the predrilled tunnel in bone (i.e., filing of the tunnel with new bone) in the Sham control than the P–Mg pins. In other words, the faster degradation rate of ZSr41 pins appeared to match the growth rate of new bone in the predrilled tunnel more closely than the P–Mg pins.

3.6. Surface Characterization of Dissected ZSr41 Alloy and Mg Intramedullary Pins

The characterization of ZSr41 and P–Mg intramedullary pins after they were implanted in the tibiae for 47 days are summarized in Figure 7. The montages in Figure 7a and 7b show the optical photos of the residual dissected implants in the center, SEM images at an original magnification of 50× on the top left, and corresponding elemental distribution maps for Mg, Ca, and P obtained through EDS. The SEM images show that ZSr41 and P–Mg pins were both corroded with degradation products on the surface. The EDS elemental distribution maps revealed the deposition of Ca and P in vivo, and the presence of Mg; the elements of Ca and P on the surface of the ZSr41 appeared to be more than P–Mg pins collected after the 47-day implantation. EDS surface elemental composition analysis in Figure 7c confirmed the presence of Zn and Sr on the residual ZSr41 pin but not on P–Mg, similar C and O content on both dissected implants, and a higher atomic ratio of Ca/P (at.% of Ca/at. % of P) for ZSr41 than P–Mg. Specifically, the ZSr41 pin had (at. %) 49.91% C, 39.57% O, 3.02%

Mg, 0.73% Zn, 0.03% Sr, 3.18% Ca, 2.84% P, and 0.72% Na, Cl, and K on the surface; the P–Mg pin had 53.65% C, 37.97% O, 4.80% Mg, 1.30% Ca, 1.77% P, and 0.51% Na, Cl, and K on the surface. Based on these EDS values of surface compositions, the Ca/P atomic ratios for the ZSr41 and P–Mg samples were calculated to be 1.12 and 0.73, respectively. Additionally, XRD analysis in Figure 7d confirmed crystalline Mg, $Mg_{17}Sr_2$, $Mg(OH)_2$, $Ca(OH)_2$ and HA on the surface of the dissected ZSr41 alloy and crystalline Mg, $Mg(OH)_2$, $Ca(OH)_2$, HA, and $Mg_3(PO_4)_2$ on the surface of the dissected P–Mg. A reference spectrum for HA in the rat tibia (i.e., crushed bone into fine powder) is included in Figure 7d to show the overlap of HA peaks with the XRD spectra from the experimental groups of ZSr41 and P–Mg.

3.7. Elemental Mapping at the Implant–Tissue Interface

Figure 8 summarizes results for elemental mapping analysis on dissected tibia cross sections to characterize the implant–tissue interface at 47 days of postsurgery. The montage in Figure 8a shows SEM images at an original magnification of 50×, and corresponding EDS elemental distribution maps for Mg, Zn, Sr, Ca, and P obtained from resin-embedded cross sections that were cut transversely at the mid-diaphysis of the proximal tibia at a distance of 5 mm from the tibial plateau. The SEM image and EDS map of Mg for ZSr41 showed that, at this anatomical location, the ZSr41 intramedullary pin was completely degraded and resorbed; and the intensities of Mg in the bone tunnel and cortical bone for ZSr41 were slightly higher than those of the Sham control. In contrast, the SEM image and EDS map of Mg for P–Mg showed the cross-section of the residual P–Mg intramedullary pin, as indicated by the white arrow in Figure 8a. The presence of Mg at the peri-implant bone region surrounding the P–Mg pin was not visible in the EDS map of Mg Ka, mainly because the drastically higher Mg content in the pin masked the lower Mg content in the surrounding bone. The EDS map of Mg for the Sham control confirmed the expected presence of Mg in the natural bone and showed its distribution in bone. Elemental distribution maps of Zn and Sr for all groups confirmed the presence of these two elements in the natural bone; the peri-implant region surrounding the ZSr41 pin showed slightly higher intensities of Zn and Sr than the Sham control and the P–Mg group. Elemental distribution maps of Ca and P for ZSr41 confirmed extensive peri-implant bone remodeling and deposition of Ca and P in the newly formed bone region in response to the degradation of the ZSr41 intramedullary pin. The Ca and P maps for P–Mg group showed a thin mineralized layer with Ca and P at the implant-tissue interface in the intramedullary bone tunnel, but almost no Ca and P signals were detected beyond this thin layer until the cortical bone region. The Ca and P maps for the Sham control confirmed the expected distribution of Ca and P minerals in the cortical and trabecular bone. Furthermore, EDS point analyses were performed in triplicate in the regions of interest to determine the quality of peri-implant bone minerals using the Ca/P atomic ratio as an indicator. EDS point analyses were carried out in the cortical bone region for all groups as indicated by the white stars in the EDS maps of P. EDS point analyses were also performed on the new bone formed around the ZSr41 implant, as indicated by the white arrowheads in the EDS maps of P, but not for the P–Mg group and the Sham control because new bone formation in the trabecular bone region was not evident for these two groups at 47 days of postsurgery. The Ca/P ratios from EDS point analyses are summarized in Figure 8b. ANOVA confirmed statistically significant

differences in the mean Ca/P ratios of the mineralized bone regions of interest [$F(3, 8) = 32.01$, $p = 8.34 \times 10^{-5}$]. Post hoc pairwise comparisons showed a significantly higher Ca/P ratio ($p < 0.001$) for the new bone formed around the ZSr41 intramedullary pin (1.56 ± 0.04) than the cortical bone surrounding the ZSr41 pin (1.25 ± 0.03); the Ca/P ratio in the cortical bone surrounding the P–Mg pin (1.55 ± 0.03) was significantly greater ($p < 0.01$) than that of the Sham control (1.39 ± 0.07).

3.8. Histological Evaluations of the Proximal Tibia

Figure 9 shows the optical images of representative histology sections of calcified bone region in the proximal tibia at 47 days of postsurgery. Longitudinal sagittal and transverse sections were embedded in PMMA and stained with either toluidine blue (blue stains for cell nucleus and structure, purple stains for collagen, and gray stains for bone) or Goldner's trichrome (green stains for mineralized bone, red stains for unmineralized osteoid, and brownish-gray stains for bone marrow cells).

Figure 9a shows the images of longitudinal sagittal sections of the proximal tibia for the ZSr41 and P–Mg groups, and the Sham control at an original magnification of 2.5×. The toluidine blue-stained longitudinal sections from the ZSr41 and P–Mg groups confirmed the presence of hydrogen-gas-induced cavities in the peri-implant region as indicated by red arrows where bone marrow cells were absent. For ZSr41 group, more gas pockets spread toward the cortical bone region; and for P–Mg group, larger gas pockets were observed in the trabecular region inside the bone tunnel. In contrast, the trabecular bone tunnel of the Sham control showed a healthy amount of bone marrow cells without gas pockets. The small vacancies in the bone tunnel of the Sham control are artifacts of chemical treatment during section preparation and pertain to healthy amounts of adipose cells;[52] adipose cell vacancies were observed in the bone tunnel of P–Mg group and Sham control, but not in the ZSr41 group. The Goldner's trichrome-stained longitudinal sections for the ZSr41 group confirmed extensive bone remodeling and new bone formation, as indicated by the white arrowhead, in response to the degradation of the ZSr41 intramedullary pin. Moreover, unmineralized osteoid was observed in the bone tunnel adjacent to the P–Mg implant, as indicated by the black arrowhead. Comparisons of the trabecular bone region of all groups showed that the distribution of trabeculae in the ZSr41 and P–Mg groups was not uniform, in contrast to the normal trabeculae distribution in the Sham control; the distribution of the trabeculae appeared to be disrupted near the gas pockets. Interestingly, the ZSr41 group showed more newly formed trabeculae than the P–Mg group.

Figure 9b shows the images of transverse sections of the proximal tibia at 6 mm away from the tibia plateau for the ZSr41 and P–Mg groups, and the Sham control at an original magnification of 2.5×. The transverse sections (both stains) confirmed extensive bone remodeling in the ZSr41 and P–Mg groups, with bone tunnel enlargement and hydrogen-gas-induced cavity formation, but not in the Sham control group. Furthermore, the annular cortical bone structure showed discontinuity and/or thinning in the ZSr41 and P–Mg groups, but not in the Sham control group. Analysis of cell structure did not show abnormal enlargement of cells, indicating the growth observed in the ZSr41 and P–Mg groups was not hypertrophic. The Goldner trichrome-stained transverse sections confirmed circumferential

peri-implant remodeling of mineralized bone in response to the degradation of the ZSr41 intramedullary pin, as indicated by white arrowheads. Bone remodeling inside the bone tunnel was also observed for the P–Mg group but to a lesser extent when compared with the ZSr41 group. Furthermore, unmineralized osteoid was observed in the bone tunnels for both ZSr41 and P–Mg groups as indicated by black arrowhead, but not in the Sham control. The presence of unmineralized osteoids in close proximity to the implant (or where the implant was originally placed) and new bone formation around the implant in the bone tunnels indicated that both ZSr41 and P–Mg implants stimulated peri-implant bone formation.[53] Additionally, in all cases, infiltration of inflammatory cells was not found.

3.9. Degradation Rates of ZSr41 alloy and Mg Intramedullary Pins in Vitro and in Vivo

Figure 10 summarizes the in vitro and in vivo degradation rates measured in this study, along with a comparison with the in vitro degradation rates previously published for ZSr41 and P–Mg. Figure 10a shows a scatter plot of ZSr41 and P–Mg implant volume V_i (measured from 3D VOIs reconstructed from μCT images) as a function of time (in days) during the 47-day implantation period. The linear-fitted curves for each group showed the decreasing trend in implant volume over time and highlighted the difference in initial implant volume (V_0). The inset in Figure 10a shows a scatter plot with a normalized implant volume (relative to V_0) as a function time (in weeks). The linear-fitted curve of the normalized volume highlights the faster degradation rate of ZSr41 (-0.12 cm^3 cm^{-3} weeks^{-1}; $R^2 = 0.99$) when compared with P–Mg (-0.07 cm^3 cm^{-3} weeks^{-1}; $R^2 = 0.95$). Extrapolation of these curves indicated that the ZSr41 and P–Mg intramedullary pins will completely degrade in 8 and 14 weeks, respectively, when implanted in the bone tunnel of rat tibia.

Figure 10b shows the average daily degradation rates for the ZSr41 and P–Mg pins analyzed in this study (both in vitro and in vivo) and normalized by the corresponding V_0. ANOVA confirmed statistically significant differences in the average daily degradation rates relative to V_0 [$F_{(3, 12)} = 177.34$, $p = 3.35 \times 10^{-10}$]. Post hoc pairwise comparisons showed that the in vivo average daily degradation rates of ZSr41 (35.64 ± 2.67 mg cm^{-3} d^{-1}) and P–Mg (16.24 ± 1.83 mg cm^{-3} d^{-1}) were both significantly higher ($p < 0.001$) than their respective in vitro degradation rates in the BMSC/DMEM system (24.39 ± 1.58 mg cm^{-3} d^{-1} for ZSr41 and 3.79 ± 0.52 mg cm^{-3} d^{-1} for P–Mg). Additionally, the average daily degradation rates of ZSr41 from both in vitro and in vivo measurements was significantly higher ($p < 0.001$) than P–Mg in the corresponding conditions.

Considering that corrosion rates are typically associated with exposed surface area,[24,27,54] the average daily degradation rate was also calculated relative to SA_0 of the ZSr41 and P–Mg pins, and the results are shown in Figure 10c. ANOVA confirmed statistically significant differences in the average daily degradation rates relative to SA_0 [$F_{(3, 12)} = 199.79$, $p = 1.66 \times 10^{-10}$]. Post hoc pairwise comparisons showed that the *in vivo* average daily degradation rates of ZSr41 (0.98 ± 0.08 mg cm^{-2} d^{-1}) and P–Mg (0.39 ± 0.04 mg cm^{-2} d^{-1}) were both significantly higher ($p < 0.001$) than their respective in vitro degradation rates in the BMSC/DMEM system (0.69 ± 0.04 mg cm^{-2} d^{-1} for ZSr41 and 0.09 ± 0.01 mg cm^{-2} d^{-1} for P–

Mg). Additionally, the average daily degradation rate of ZSr41 was significantly higher ($p < 0.001$) than P–Mg according to both in vitro and in vivo measurements.

Figure 10d shows a comparison between the average daily degradation rates relative to SA_0 measured in this study and in vitro degradation rates of ZSr41 in other in vitro cell culture systems with respective cell types reported previously.[8,10,11] Although the comparative figure includes several variables, in the context of alloy design and optimization, this comparison illustrates the range of in vitro degradation rates of the ZSr41 alloy under different experimental conditions. Collectively, Figure 10d shows a lower in vitro degradation rate for the rolled and aged ZSr41 sheets than the as-drawn pins in the same BMSC/DMEM culture system, suggesting that optimization of processing methods and parameters could further reduce the ZSr41 alloy degradation rate to meet the requirements for different medical applications.

4. DISCUSSIONS

Many factors could affect the in vitro and in vivo degradation of Mg-based materials, and their cytocompatibility and biocompatibility in vitro and in vivo. The in vitro factors such as the culture system and method used and the in vivo factors such as the anatomical locations of implantation and animal model used could all influence the results, in addition to intrinsic material factors such as composition, microstructure, processing conditions, sample dimension and geometry, and sample surface conditions, etc. Thus, it is important to closely examine and further discuss the key factors that influenced the in vitro and in vivo degradation, cytocompatibility and biocompatibility of as-drawn ZSr41 and P–Mg intramedullary pins, hopefully enhancing our understanding of Mg-based materials for potential clinical translations.

Experimentally, all the samples were sterilized in the same fashion in this study, using a standard autoclave gravity cycle at 122 °C for 30 min. It is important to use the same sterilization method when preparing samples for in vitro and in vivo studies because different sterilization methods could cause different changes in Mg-based samples, affecting biological responses in vitro and in vivo. Specifically, autoclave and gamma (γ) radiation are the most widely adapted sterilization methods for in vivo studies and for medical implants and devices used clinically. Autoclave sterilization causes surface oxidation of Mg-based materials because the standard autoclave involves the temperature in the range of 121–134 °C and 100% humidity. In comparison, γ radiation could cause overall change in grain structures of Mg alloys, thus affecting their mechanical, biological and degradation properties afterward.[55] Ultraviolet (UV) irradiation is widely used for disinfecting samples for in vitro studies and does not cause significant changes on Mg-based metals; however, it is not sufficient for sterilizing materials for in vivo studies and clinical use. Thus, we selected autoclave as our sterilization method for all samples used for in vitro and in vivo studies to maximize consistency of samples and comparability of results. Ideally, the duration of in vitro culture and in vivo implantation of Mg-based materials should be kept the same for direct comparison. However, repeatability of in vitro cell studies is a concern when the culture time is extended to weeks because cells may change their phenotype and functions, especially primary cells such as BMSCs used in this study. Moreover, BMSCs

reached complete confluence after 72 h of culture, not practical for further extending the culture time. To address this difference between the duration of in vitro culture and in vivo implantation, the results were normalized by time (per day).

4.1. Degradation Behaviors of ZSr41 Alloy and P–Mg Pins As Intramedullary Implants in Vitro and in Vivo

To our knowledge, this is the first report on the in vitro and in vivo degradation of as-drawn ZSr41 wires in comparison with as-drawn P–Mg. The degradation (i.e., corrosion) rate of the ZSr41 alloy was likely mediated by the electrochemical behavior between the α-Mg matrix and secondary-phase precipitates; the dimension, composition, and dispersion of these secondary phases play important roles in the alloy degradation. Previous studies indicated that crystalline Mg–Zn–Sr alloys showed segregation of Zn and Sr predominantly in the precipitated phases accompanied by an α-matrix with ~4 wt % Zn.[7,56,57] Specifically, previous studies[7] confirmed the presence of $Mg_{17}Sr_2$, a binary $Zn_{13}Sr$ phase, and a variety of Mg–Zn binary phases in as-cast Mg-4Zn-1Sr alloy sheets through EDS and XRD analysis. The EDS and XRD results from this study (Figure 1a and 1a′) on as-drawn ZSr41 pin confirmed the presence of the $Mg_{17}Sr_2$ phase and a binary Mg–Zn phase (Mg_7Zn_3). In the rolled and heat-treated Mg–4Zn–xSr ternary alloys, the Zn/Sr atomic ratio played an important role in the composition and morphology of the β-phases, both of which are critical factors affecting microgalvanic corrosion (i.e., corrosion resistance of the alloy).[10] Microstructurally, previous studies[7,10] showed that the secondary phases in rolled and heat-treated Mg–4Zn–1Sr alloy sheets consisted of dispersed spherical particulates of a few microns in diameter. In contrast, the microstructure of the as-drawn ZSr41 pins used in this study showed interconnected networks of secondary β-phase (white web-like structures; Figure 1a). Further discussions on the evolution of the microstructure during solidification and processing, characterization of grains and secondary phases, and mechanical properties of the Mg–Zn–Sr alloy system can be found in refs 7, 56, and 57, and a thermodynamic evaluation with phase diagrams was reported in the ref 58. Controlling the microstructure and secondary phases in the ZSr41 pins could improve or modulate their degradation properties for biomedical applications. This would require further investigations on the β-phase mediated corrosion in Mg alloys and the relationships among the microstructures of the ZSr41 alloy, processing parameters, and degradation properties. Addition of alloying elements such as Zn and Sr induced the formation of intermetallic compounds, which could increase nucleation sites for oxide formation on the surface during autoclave.[7] Surface oxide layer could either slow down Mg degradation through inhibiting cathodic reactions or increase microgalvanic corrosion via making the β phase more cathodic. Moreover, alloy composition and surface property (i.e., presence or absence of oxides) could increase or decrease the degradation rate, which was found dependent on the environmental conditions as well.[31] In the future studies, we suggest to perform more detailed microstructural analyses using transmission electron microscopy to determine the composition, morphology, and distribution of the β-phases, and establish a model to quantify the relationships among microstructure, processing, and standard electrode potential, in order to control microgalvanic corrosion at the microstructure level.

This study showed that the in vitro degradation rate of the ZSr41 pins in the BMSC/DMEM culture system was significantly higher than the P–Mg pins. However, the rolled ZSr41 sheet showed a similar in vitro degradation rate to the rolled P–Mg sheet at the same thickness of 1 mm in the BMSC/DMEM culture system.[11] This suggests that the processing conditions, microstructures, and geometry and dimension of Mg alloy samples could affect the in vitro degradation rates significantly. Although the results from PDP measurements and Tafel extrapolation (Figure 2) showed small differences in E_{corr} and J_{corr} values for the as-polished ZSr41 and P–Mg pins, we could consider they had similar characteristics in the initial corrosion response in the electrochemical testing. Specifically, the E_{corr} value for ZSr41 pin was statistically lower than P–Mg (Figure 2b), but the difference was small (less than 0.06 V); and the J_{corr} value did not show statistically significant differences (Figure 2c). ASTM standard G102-89 described the corrosion rate (CR, mm/year) of the samples directly proportional to J_{corr} value, as shown in this equation

$$CR = \frac{J_{corr} \cdot K \cdot EW}{\rho}$$

where CR is corrosion rate, J_{corr} is corrosion current density, K is constant for converting units, EW is equivalent weight, and ρ is density of corroding samples. The difference between the corrosion rates calculated from PDP measurements and the immersion degradation rates was expected, because the PDP measurements provided the initial corrosion behaviors immediately upon exposure to rSBF and the BMSC/DMEM culture systems more closely simulated in vivo physiology conditions in a prescribed culture period with the presence of relevant ions, proteins and cells. The ions, proteins and cells all play important roles in degradation of Mg and Mg alloys.[31,59]

The results from the in vitro degradation in the BMSC/DMEM culture system showed mass gain for the first day (D1) and then mass loss at D2 and D3 for the ZSr41 pin, but P–Mg pin showed mass gain for the first 2 days and mass loss at D3 (Figure 3e). Final mass of the ZSr41 and P–Mg pins included the insoluble degradation products deposited on the sample surface. The sample mass gain indicated the formation of degradation layer on the surface of the ZSr41 and P–Mg pins, which was also confirmed in SEM images in Figure 4. Over the 3-day in vitro culture period, the ZSr41 pin showed greater mass loss, and higher pH and $[Mg^{2+}]$ in the culture media than the P–Mg pin (Figure 3e–g), which indicated a significantly higher in vitro degradation rate of ZSr41 than P–Mg. Nevertheless, the $[Mg^{2+}]$, $[Zn^{2+}]$, and $[Sr^{2+}]$ in the media for the ZSr41 group (Figure 3g–3i) were still well below the therapeutic daily dosages (TDD) and LD_{50} reported in literature.[8] Qualitatively, surface characterization of the ZSr41 and P–Mg pins after the 3-day in vitro culture (Figure 4) showed more degradation products with a higher O content and a higher Ca/P ratio, and less cracks on the ZSr41 pin than that on the P–Mg pin; and, the crystalline phases on the surface of the ZSr41 pin were very different from that on the P–Mg pin. Interestingly, a variety of oxide and hydroxide phases, and crystalline phases of phosphates were found on the surfaces of both ZSr41 and P–Mg pins after the in vitro culture. Although the ZSr41 showed a Ca/P ratio closer to that of tricalcium phosphate (TCP; the theoretical stoichiometric Ca/P ratio

for TCP is 1.5) when compared with P–Mg, the calculated Ca/P ratio was only a rough estimate since Ca or P was found in other phases present on the surface of the ZSr41 and P–Mg pins. Overall, the surface characterization suggested that the ZSr41 pin had a different degradation mode when compared with P–Mg.

In literature, the results from the rolled and heat-treated ZSr41 sheets showed that the in vitro degradation rate of the ZSr41 alloy (Mg–4Zn–1Sr, wt %) was slower than pure Mg when incubated in r-SBF for 15 days[7] and in the hESC/mTeSR culture system for 3 days,[8] and similar to pure Mg when incubated in the HUVEC/EGM-2 culture system for 1 day,[10] in DMEM media for 3 days,[11] and in human blood and plasma for 2 h.[9] The results from these previous in vitro degradation studies for ZSr41 alloys are summarized in Figure 10d. It is likely that the differences in the in vitro degradation rates in distinct culture systems observed for ZSr41 alloys were primarily affected by the HCO_3^- ion concentration in the culture media.[11,60,61] Kirkland et al. provided a comprehensive summary of in vitro degradation rates (mg cm^{-2} day^{-1}) of various Mg-based biomaterials and the in vitro results from this study were within the range provided.[54] In fact, the in vitro degradation rates for the ZSr41 pins and P–Mg control obtained in this study ranked in the middle and lower range, respectively, when compared with a variety of Mg-based biomaterials incubated for 3, 7, and 14 days in minimum essential medium (MEM) without serum.[54]

The in vivo degradation rate of the ZSr41 wires was studied for the first time as compared with as-drawn P–Mg wires. When used as intramedullary pins placed in rat tibiae for 47 days, the degradation rate of ZSr41 pin was significantly higher than the P–Mg control. The results from weekly μCT scans (Figure 5a) along with corresponding reconstructed 3D VOIs (Figure 6h) showed a faster degradation rate for the ZSr41 intramedullary pins than the P–Mg control. Quantification of volume change at each time point (Figure 6i) confirmed a statistically faster degradation rate for ZSr41 pins than the P–Mg control starting at day 12. The oxide formation on the surface of ZSr41 pins during autoclave could be one of the reasons for the faster degradation rate, because the oxides could increase microgalvanic corrosion. Moreover, when coupled with certain environmental factors, the oxides on the surface could either increase or decrease the degradation rates of Mg alloys, depending on the surrounding ions, proteins and cells.[31,62] Even though Zn should theoretically improve the corrosion resistance when alloyed in Mg alloys, the microstructures and surface conditions of the samples could be coupled with the environmental factors, leading to different outcome. Therefore, the ZSr41 wires should be further optimized in the future to modulate the degradation rate. The pin volume reduction measured in situ was also confirmed through analyses of dissected implants (Figure 7a and 7b), elemental mapping at the tissue-implant interface (Figure 8), and histological evaluation (Figure 9). Both qualitative and quantitative results confirmed near-complete resorption of the ZSr41 intra-medullary pin but considerable residues of the P–Mg pin. Surface characterization of the dissected implant through SEM, EDS, and XRD (Figure 7) showed the presence of Mg, $Mg_{17}Sr_2$, $Mg(OH)_2$, $Ca(OH)_2$, and HA phases for ZSr41 pins. The presence of Mg, $Mg(OH)_2$ and HA phases are in agreement with previous evaluations of Mg–Sr intramedullary implants placed in mice femora[42] and Mg–Ca intramedullary implants placed in rabbit femora.[63] The formation of $Ca(OH)_2$ and $Mg(OH)_2$ is ascribed to the alkaline conditions around ZSr41 pins. The Mg_7Zn_3 phase was not detected in XRD after in vitro

culture (Figure 4a′ and 4b′) and in vivo implantation (Figure 7d); one possibility is that Mg_7Zn_3 phase interacted with the chemicals in the surrounding environment to form other phases. Overall, the degradation of ZSr41 and P–Mg released a large amount of Mg^{2+} ions into the surrounding tissue, induced the formation of $Mg(OH)_2$, attracted calcium and phosphate ions from the surrounding environment, and promoted deposition of calcium and phosphate phases. The process for forming hydroxyapatite (HA) and magnesium phosphates on metal surface has been reported previously.[64]

The in vivo average daily degradation rates of both ZSr41 and P–Mg intramedullary pins were significantly higher than their respective degradation rates in vitro. These results are in agreement with previous studies that reported higher in vivo degradation rates, when compared with their in vitro (via immersion) counterparts, for rolled Mg-2Sr alloy[42] and extruded Mg-6Zn alloy[65] intramedullary implants, and for high-purity Mg (99.99 wt %) transcortical screws.[43] Specifically, for the Mg-2Sr alloy, Gu et al. compared the in vitro degradation rate obtained from the immersion of implants in Hank's solution during 500 h of immersion with the in vivo degradation rate obtained from implantation in the femoral shaft of C578L/6 mice for 4 weeks.[42] For the Mg-6Zn alloy, Zhang et al. compared the in vitro degradation rate obtained from the immersion of implants in SBF during 3 and 30 days with the in vivo degradation rate obtained from implantation in the femoral shaft of New Zealand white rabbits for 14 weeks.[65] Similarly, Han et al. compared the in vitro degradation rate obtained from the immersion of implants in modified SBF during 4 and 16 weeks with the in vivo degradation rate obtained from transcortical implantation in fractured femoral condyles of New Zealand white rabbits for 4 and 24 weeks.[43] However, some literature reported the opposite trend; that is, the in vivo degradation rate is slower than the degradation rate measured via in vitro immersion. A recent comprehensive review by Martinez Sanchez et al. showed that for many Mg alloys, the in vivo degradation rate could be as much as 9 times lower when compared with the results from in vitro immersion tests.[27] Martinez Sanchez et al. pointed out the intrinsic effects of the implantation site on the measured in vivo degradation rate. In addition to the importance of implantation site, we believe the experimental methods, time periods, sample dimension and geometry, and sample fabrication parameters should also be considered when discussing or comparing the degradation rate or corrosion rate. In this study, as well as those studies used for comparison, [42,43,65] the Mg-based implants were placed in the anatomical regions rich in vasculature, which very likely accelerated the in vivo degradation and resulted in a greater degradation rate being measured. Willbold et al. showed that the in vivo degradation of AZ31 screws was largely dependent on the implantation site.[66] More and more literature supported a faster corrosion rate of Mg-based implants in the trabecular region, which is rich in vasculature and body fluids, when compared with the cortical bone region.[39,40,42,67,68] Faster degradation in intramedullary areas than cortical area was attributed to the fact that enhanced vascularization of bone marrow could make the removal of degradation products (e.g., OH^- ions, Mg^{2+} ions, etc.) more rapidly, and thus accelerate degradation reactions.[39] Moreover, Mg^{2+} ion can improve vascular formation during new bone formation. Extracellular Mg^{2+} ion is a receptor-mediated chemoattractant for endothelial cells, which can enhance endothelial cell migration and proliferation via signal transduction pathway modulated by angiogenic factors.[69,70] The methods used for measuring the in vitro and in vivo degradation

in this study were in agreement with the recommendations in literature[27] for providing accurate and continuous corrosion measurements. Moreover, the comparison between the in vitro and the in vivo degradation rates in this study contributed to the field-wide efforts on bridging the gap between the in vitro and in vivo results.

To our knowledge, this is the first report on the in vivo implantation of ZSr41 intramedullary pins. The as-drawn ZSr41 pins are estimated to resorb completely in 8 weeks in bone marrow cavity in vivo, probably faster than the design criteria for most orthopedic fixation devices. However, it is important to mention that the processing conditions for the ZSr41 alloy wire could be further optimized to control the microstructure and modulate the degradation rates; surface modifications or coatings on the ZSr41 alloy may be necessary to further reduce the alloy degradation to meet the requirements for specific application. Additionally, faster degrading alloys may be needed for pediatric applications or other clinical scenarios outside of orthopedics; and specific discussions with clinicians in different medical specialties are essential toward potential clinical translation of Mg-based biomaterials. For the future, we hope to integrate experimental methods with computational modeling to elucidate the correlations between the in vitro and in vivo results. If we could establish more effective screening methods to identify the best alloy candidate before in vivo studies, we could potentially reduce the use of animals in research and accelerate clinical translation.

4.2. Cytocompatibility of As-Drawn ZSr41 Pins in Exposure Culture with BMSCs

The results of the 3-day in vitro evaluation of cytocompatibility of ZSr41 pins in exposure culture with BMSCs (Figure 3) showed that although the ZSr41 pin showed signs of faster degradation than the P–Mg pin as early as day 1, no statistically significant differences in the BMSC density between the ZSr41 and P–Mg groups were detected at D1, D2, and D3 over the 3-day culture period. The difference between the ZSr41 group and the BMSC reference in the BMSC densities at location R_1 at D3 was considered trivial because BMSCs reached confluence as shown in fluorescence images in Figure 3a. In fact, during the 3-day exposure culture with the ZSr41 pins in this study, solubilized $[Mg^{2+}]$, $[Zn^{2+}]$, and $[Sr^{2+}]$ in the media (Figure 3g–3i) were all below their respective therapeutic daily dosages (TDD) ($[Mg^{2+}]$ = 24–40 mM,[71] $[Zn^{2+}]$ = 0.9 mM,[72] $[Sr^{2+}]$ = 5.9 mM[73]) and LD50 ($[Mg^{2+}]$ = 50–73 mM,[72] $[Zn^{2+}]$ = 3.7 mM,[74] $[Sr^{2+}]$ = 33.8 mM[75]) reported in literature.[8] Previous studies demonstrated the cytocompatibility of rolled and heat-treated sheets of Mg–Zn–Sr alloys with H9-hESCs,[8] fibroblasts,[9,57] HUVECs,[10] osteoblasts,[76] and BMSCs.[11]

Previously, our group introduced the direct in vitro culture method designed for Mg-based materials to study interactions and possible cytotoxic effects at the cell-biomaterial interface.[24] In the direct culture method, cells are seeded directly onto the sample surface, but also seeded surrounding the sample; by doing so, we can evaluate cells (i) in direct contact with the sample, and (ii) in indirect contact with the sample. Thus, the direct culture method complements traditional immersion-based methods (i.e., ISO 10993) and provides a more physiologically relevant in vitro model to study Mg-based biomaterials. In a previous study, we investigated the cytocompatibility of rolled and aged Mg–4Zn–xSr (x = 0.15, 0.5, 1.0, and 1.5 wt %) alloy sheets using the direct culture method with BMSCs.[11] The results

from[11] showed that the Mg–4Zn–1Sr alloys (i.e., ZSr41) were cytocompatible with BMSCs both in direct and indirect contact with the samples for up to 3 days. In fact, there were no significant differences in BMSC adhesion density when compared with the glass reference and cells-only positive control. It should be pointed out that the degradation rate of the rolled and aged ZSr41 sheets in DMEM was approximately one-third as compared with that of the as-drawn pins (Figure 10d). Therefore, further optimization of the processing parameters for the as-drawn pins of Mg–Zn–Sr crystalline ternary alloys should lead to slower degradation rates and better cytocompatibility.

4.3. Host Response to As-Drawn ZSr41 Intramedullary Pins in Vivo

Although the as-drawn ZSr41 pins under current processing parameters degraded faster than the typical expectation for an orthopedic implant, the host responses to a fast-degrading alloy provided new insights of interest to the field. Specifically, the implant degradation, gas pocket formation, and peri-implant bone volume and bone quality are closely related and their relationships are of importance for advancing the field of biodegradable metallic implants.

The capability of Mg-based biomaterials in increasing peri-implant bone formation has been demonstrated in different animal models.[39,42,43,63,67,68,77–80] Both intrinsic material properties and anatomical locations in animal models could affect the degradation of Mg-based implants and host responses in vivo.[39,80] The as-drawn ZSr41 intramedullary pins showed a faster degradation rate than P–Mg when implanted in the marrow cavity of rat tibia, and the host responses to the ZSr41 pins represented a scenario at which the degradation rates of Mg-based implants approached the upper threshold.[27] Host responses to fast-degrading Mg alloys have not been well studied yet. To our knowledge, only Kraus et al. monitored a rapid-degrading Mg-alloy implant until complete degradation and reported the associated host responses and bone remodeling previously.[39] Kraus et al. reported both ion-induced bone formation and hydrogen-gas-induced damage during extensive bone remodeling as a result of rapid degradation of the ZX50 alloy (Mg-5Zn-0.25Ca-0.15Mn, wt %). After complete resorption of the ZX50 implant at 12 weeks, near-complete bone homeostasis was recovered at 24 weeks. In this study, the fast degradation of the ZSr41 implant induced both gas pocket formation and new bone formation, and showed signs of extensive peri-implant bone remodeling.

Hydrogen gas released during the fast degradation of ZSr41 intramedullary pins induced cavities in the bone tunnel and peri-implant cortical bone. The formation of hydrogen gas pockets inside the bone tunnel was observed via μCT scans for both ZSr41 and P–Mg implant groups (Figure 5a). Hydrogen gas induced cavities in the peri-implant cortical bone were visible in the 3D reconstructed bone VOIs (Figure 6a). Figure 5a is merely one 2D cross-section of each reconstructed 3D image at representative time points. Generally, there were more cavities in the cortical bone of the ZSr41 group and more cavities in the bone tunnel of the P–Mg group. Histological analyses at the day 47 postimplantation (Figure 9) confirmed this. Specifically, both toluidine blue and Goldner trichrome stained sections confirmed the presence of cavities in the peri-implant cortical bone region for the ZSr41 and P–Mg groups, the presence of acellular pockets in the bone tunnel for both ZSr41 and P–Mg

groups, and lack of inflammatory cells in both groups. Other studies also showed the degradation of Mg-based implants caused damage to the peri-implant cortical bone, although the authors attributed some of the occurrences to segmentation artifacts.[42,80] Kraus et al. and Wang et al. studied Mg-alloys as implant materials and reported the effects of gas accumulation on bone healing; and both studies indicated a lack of inflammatory cell infiltration.[39,44] This is consistent with published literature for a variety of Mg alloys evaluated for up to 36 weeks postimplantation,[39,44,66–68,79,81] suggesting Mg alloys generally should not induce inflammatory responses in vivo. Kraus et al. observed substantial peri-implant gas and gas-induced cavity formation via μCT scans, 3D reconstructions, and histological analysis during 4–12 weeks of postimplantation. Kraus et al. suggested that accumulation of hydrogen gas pressure induced mechanical stress during the cortical bone remodeling, resulting in altered callus formation. When most of the Mg alloy implant was resorbed and hydrogen gas evolution reduced after week 12, Kraus et al. observed quick bone remodeling and healing of bone defects from week 12–24 and near-complete restoration of bone at week 24.[39] In a separate study, Wang et al. reported that hydrogen gas formation caused cavity formation in peri-implant cortical bone with the largest cavities occurring 8–12 weeks post implantation of Mg–Zn–Zr alloys. At 24 weeks of post-implantation, μCT scans, 3D reconstructions, and histological analyses confirmed an improvement in trabecular and cortical bone characteristics along with a reduction in local bone damage. The authors indicated that the gradually disappearing gas cavities were filled with newly regenerated bone, cartilage, and fibrous tissue.[44] Wang et al. pointed out that the main concern regarding hydrogen gas formation did not pertain to bone remodeling (which is achieved following cavity formation), but rather to the loosened contact at the implant-tissue interface, which could reduce the effectiveness of Mg-based fixation device. Interestingly, although the time frames for cavity formation (up to week 12 postimplantation) and bone healing (12–24 weeks of postimplantation) were similar for both studies, the degradation time frames for the alloys used were drastically distinct. Specifically, the ZX50 alloy used by Kraus et al. was almost completely resorbed in 12 weeks, whereas the Mg–Zn–Zr alloy used by Wang et al. lasted well over 6 months. Therefore, the production of hydrogen gas is expected during the *in vivo* degradation of the ZSr41 and P–Mg pins, and the observed hydrogen gas formation and hydrogen-gas-induced cavities in this study are well in agreement with the studies by Kraus et al. and Wang et al. By comparison, we could speculate an onset of rapid bone remodeling following complete resorption of the ZSr41 pins (approximately 8 weeks of postimplantation). Additionally, our results showed for the first time that accumulation of degradation products (hydrogen gas or OH^- induced local alkalinity) of Mg-based biomaterials could reduce the amount of peri-implant bone marrow cells. Remarkably, despite the different degradation rates of Mg-based implant studied, in all cases reported in literature, the gas produced from the in vivo degradation of Mg-based biomaterial was gradually absorbed by the host tissue without noticeable systemic effects on animal mobility. Similarly, all animals used in this study survived with normal mobility after implantation of ZSr41 or P–Mg intramedullary pins.

Despite of hydrogen gas production, the ZSr41 group showed a significant increase in peri-implant bone volume, when compared with the P–Mg group and Sham control, according to the qualitative analyses of the in situ 2D μCT scans (Figure 5a) and the quantitative analyses

of the reconstructed 3D peri-implant bone volume (Figure 6a–d). Moreover, EDS and XRD analyses of the dissected residual ZSr41 implant confirmed HA formation on the implant surface (Figure 7), which indicated bone formation at the tissue-implant interface. The qualitative EDS analyses on resin-embedded cross sections showed new bone formation at the site of implantation and resorption for the ZSr41 pins (Figure 8a). Histological analysis of plastic-embedded sections (Figure 9) confirmed the formation of mineralized woven bone at the site where the ZSr41 implant was placed and resorbed; the presence of unmineralized osteoid at the site of implantation and resorption of the ZSr41 pin provided the evidence for osteogenesis.[53] The increased peri-implant bone volume was reported in many studies, [22,39,42–44,63,67,77–79,82] as a result of increased osteoblastic or osteoclastic activities, in response to the release of Mg^{2+} ions from the degradation of Mg-based implants. [22,39,43,63,78,79] It was suggested that reactive bone hyperplasia was the cause of increased peri-implant bone volume, in response to the degradation products of Mg-based biodegradable implants.[80] In this study, it is likely that Sr^{2+} ions released during the degradation of ZSr41 further enhanced osteoblastic activity. This was also supported by other studies on Mg–Sr alloys for orthopedic implant applications.[22,42]

While the degradation of the ZSr41 intramedullary pins caused an increase in peri-implant bone volume, Mg^{2+}, Sr^{2+}, or Zn^{2+} ion concentrations in the blood for the ZSr41 group (Figure 5b–5d, respectively) did not show any change beyond biological variations. Although some statically significant differences were detected among the ZSr41, P–Mg, and Sham groups, these slight variations in blood ion concentrations could have resulted from differences in the food intake and random biological deviations. All the ion concentrations in blood were well under therapeutic daily dosages.[8] Similarly, other studies showed that the in vivo degradation of Mg-based implants did not cause any increase in Mg^{2+} ion concentration in the blood.[42,63,67,68] In fact, previous studies also evaluated the responses of visceral organ function to the degradation of Mg-based implants and confirmed minimal/no effect on liver function and no effect on kidney function.[22,68,82] Collectively, it is reasonable to conclude that the reduced bone marrow cell density in vivo was related to the fast degradation rate induced alkalinity and H_2 gas, not to the alloying elements in the Mg–Zn–Sr alloys.

The overall bone remodeling in response to the degradation of the ZSr41 intramedullary pin can be described as a result of two parallel processes. The first is ion-induced stimulation that led to bone growth; and the second is hydrogen gas formation that led to cavity formation in bone.[39,44] Kraus et al. reported that ion-stimulated bone formation dominated over hydrogen-gas-induced cavity formation, even for rapid degrading alloys such as ZX50 that was completely resorbed in approximately 12 weeks.[39] Overall, despite of their rapid degradation rate, the ZSr41 intramedullary pins showed a net gain in peri-implant bone volume because of the stimulatory effects of Mg^{2+} ions and other metallic ions (e.g., Sr^{2+}) on osteogenesis, which is in agreement with other studies.[22,39]

Rapid degradation of ZSr41 pins did affect the quality of peri-implant bone, despite of the increase of peri-implant bone volume. Specifically, the ZSr41 implant group showed a statistically greater weight density in trabecular bone and similar weight density in cortical bone at the early time points D12 when compared with the P–Mg group (Figure 6e), but at the later time points D47, the faster degrading ZSr41 pin showed a similar weight density in

trabecular bone and statistically lower weight density in cortical bone when compared with the P–Mg group (Figure 6g). Furthermore, when the residual pins were examined at D47, the ZSr41 pin showed a higher Ca/P ratio on the surface (i.e., closer to Ca/P ratio of HA in healthy bone) than P–Mg (Figure 7). At D47, newly formed bone at and near the resorption site of ZSr41 pin in the bone tunnel showed a significantly higher Ca/P ratio than that of the old cortical bone surrounding the ZSr41 implant and the Ca/P ratio in the cortical bone of Sham control, which was similar to the Ca/P ratio in the cortical bone surrounding the P–Mg implant (Figure 8). Similarly, Gu et al. observed distinct Ca/P ratios in newly formed peri-implant bone, which they attributed to bone remodeling.[42] In addition, more new mineralized bone and unmineralized osteoid appeared at and near the resorption site of ZSr41 pin in the bone tunnel than those in the bone tunnels of P–Mg group and the Sham control (Figure 9). Collectively, the newly formed bone in the bone tunnel at and near the ZSr41 pin showed a better quality than the old cortical bone surrounding it, likely because of the Mg^{2+}, Zn^{2+}, and Sr^{2+} metallic ions released from ZSr41 pins.

Considering the general degradation reactions of Mg alloys, including ZSr41, the release rate of metallic ions is proportional to the release rate of OH^- ions and hydrogen gas. In the case of ZSr41 alloy degradation, the release of Mg^{2+}, Zn^{2+}, and Sr^{2+} ions are stimulatory for bone remodeling and beneficial for bone healing, but proportionally released OH^- ions and hydrogen gas are detrimental. On one hand, rapid release of metallic ions stimulated extensive bone remodeling, and resulted in a net gain in bone volume and high-quality new bone in the bone tunnel at and near the ZSr41 intramedullary pins. On the other hand, proportionally released OH^- ions and hydrogen gas caused adverse effects on bone marrow cells and accumulation of hydrogen gas that resulted in cavities in surrounding bone, which reduced the peri-implant cortical bone quality. Balancing these effects is critical for the success of Mg-based implants. Other studies on slower degrading Mg alloys that took more than 8 weeks to complete *in vivo* resorption did not report adverse effects on bone mineral density (BMD)[42,43] or tissue mineral density (TMD).[44] Therefore, it is necessary to reduce the degradation rates of ZSr41 pins by optimizing the processing conditions and microstructures, and/or modifying the surface by coatings, in order to harvest the beneficial effects of metallic ion release and mitigate the harmful effects of OH^- ion and H_2 gas release. Additionally, longer term evaluation in vivo is necessary to monitor the quality of remodeled bone following complete resorption of the ZSr41 implant, because it is likely that the quality of bone will continue to improve over time.

5. CONCLUSIONS

This Research Article reports for the first time the in vitro degradation of as-drawn ZSr41 pins and their cytocompatibility with BMSCs in the exposure culture, and the in vivo degradation and biocompatibility of the ZSr41 pins in rat tibiae, in comparison with P–Mg. The as-drawn ZSr41 pins showed a significantly faster in vitro degradation rate than the P–Mg control in the 3-day exposure culture with BMSCs in DMEM. Nevertheless, the Mg^{2+}, Zn^{2+}, and Sr^{2+} ions released in the BMSC/DMEM culture system were all below the therapeutic dosages, and thus cytocompatible. The in vivo degradation rate of the as-drawn ZSr41 was significantly higher than the P–Mg control when implanted in rat tibiae as intramedullary pins for 47 days. Moreover, the in vivo average daily degradation rates of

both ZSr41 and P–Mg intra-medullary pins were significantly higher than their respective in vitro degradation rates, likely because of the site of implantation in the highly vascularized intramedullary region. Although a growing body of literature on Mg-based implants supports slower degradation rates in vivo than in vitro, our results, in agreement with the other intramedullary implant studies, suggest that the implantation site is a critical factor to consider when comparing in vitro with in vivo results. Despite of rapid degradation with a complete resorption time of 8 weeks in vivo, the ZSr41 intramedullary pins showed a significant net bone growth because of stimulatory effects of the metallic ions released. However, proportionally released OH$^-$ ions and hydrogen gas caused adverse effects on bone marrow cells and resulted in cavities in surrounding bone. Thus, properly engineering the degradation rates of Mg-based implants is critical for harvesting beneficial properties while preventing adverse biological responses. One approach is to optimize the processing parameters and another approach is to modify the surface, for example, applying coatings on the surface. It is necessary to explore both approaches to reduce the degradation rate of as-draw ZSr41 wires for skeletal implant applications.

Acknowledgments

References

1. Staiger MP, Pietak AM, Huadmai J, Dias G. Magnesium and its alloys as orthopedic biomaterials: A review. Biomaterials. 2006; 27(9):1728–1734. [PubMed: 16246414]

2. Witte F, Hort N, Vogt C, Cohen S, Kainer KU, Willumeit R, Feyerabend F. Degradable biomaterials based on magnesium corrosion. Curr Opin Solid State Mater Sci. 2008; 12(5–6):63–72.

3. Zheng YF, Gu XN, Witte F. Biodegradable metals. Mater Sci Eng, R. 2014; 77(0):1–34.

4. Hermawan H, Dubé D, Mantovani D. Developments in metallic biodegradable stents. Acta Biomater. 2010; 6(5):1693–1697. [PubMed: 19815097]

5. Amini AR, Wallace JS, Nukavarapu SP. Short-Term and Long-Term Effects of Orthopedic Biodegradable Implants. J Long-Term Eff Med Implants. 2011; 21(2):93–122. [PubMed: 22043969]

6. Jiang Y, Jia T, Wooley PH, Yang SY. Current research in the pathogenesis of aseptic implant loosening associated with particulate wear debris. Acta Orthop Belg. 2013; 79(1):1–9. [PubMed: 23547507]

7. Guan RG, Cipriano AF, Zhao ZY, Lock J, Tie D, Zhao T, Cui T, Liu H. Development and Evaluation of a Magnesium-Zinc-Strontium Alloy for Biomedical Applications – Alloy Processing, Microstructure, Mechanical Properties, and Biodegradation. Mater Sci Eng, C. 2013; 33(7):3661–3669.

8. Cipriano AF, Zhao T, Johnson I, Guan RG, Garcia S, Liu H. In vitro degradation of four magnesium–zinc–strontium alloys and their cytocompatibility with human embryonic stem cells. J Mater Sci: Mater Med. 2013; 24(4):989–1003. [PubMed: 23361966]

9. Nguyen TY, Cipriano AF, Guan RG, Zhao ZY, Liu H. In vitro interactions of blood, platelet, and fibroblast with biodegradable Magnesium-Zinc-Strontium alloys. J Biomed Mater Res, Part A. 2015; 103(9):2974–2986.

10. Cipriano AF, Sallee A, Tayoba M, Cortez Alcaraz MC, Lin A, Guan RG, Zhao ZY, Liu H. Cytocompatibility and Early Inflammatory Response of Human Endothelial Cells in Direct Culture with Mg-Zn-Sr Alloys. Acta Biomater. 2017; 48:499–520. [PubMed: 27746360]

11. Cipriano AF, Sallee A, Guan RG, Lin A, Liu H. A Comparison Study on the Degradation and Cytocompatibility of Mg-4Zn-xSr Alloys in Direct Culture. ACS Biomater Sci Eng. 2017; 3(4): 540–550.

12. Trumbo P, Yates AA, Schlicker S, Poos M. Dietary reference intakes: vitamin A, vitamin K, arsenic, boron, chromium, copper, iodine, iron, manganese, molybdenum, nickel, silicon, vanadium, and zinc. J Am Diet Assoc. 2001; 101(3):294–301. [PubMed: 11269606]

13. Solomons NW. Mild human zinc deficiency produces an imbalance between cell-mediated and humoral immunity. Nutr Rev. 1998; 56:27–28. [PubMed: 9481116]

14. Prasad AS. Zinc: An overview. Nutrition. 1995; 11:93–99. [PubMed: 7749260]

15. Heyneman CA. Zinc deficiency and taste disorders. Ann Pharmacother. 1996; 30(2):186–187. [PubMed: 8835055]

16. Mao L. Effect of microelement Zn on the generation of immunocyte. Microelement and Health Research. 2002; 19(2):72–74.

17. Apostolidis N, Paradellis T, Karydas A, Manouras A, Katirtzoglou N, Mayopoulou-Symvoulidou D. Calcium and strontium metabolic studies in patients on CAPD. Peritoneal Dial Int. 1998; 18(4): 410–414.

18. Marie PJ. Strontium ranelate: A physiological approach for optimizing bone formation and resorption. Bone. 2006; 38(2):10–14.

19. Liang Z, Yang P, Li Z. Development of studying on the relationship of Sr with cardiovacular diseases. People's Surgeon. 2007; 50(12):768–769.

20. Meunier PJ, Roux C, Seeman E, Ortolani S, Badurski JE, Spector TD, Cannata J, Balogh A, Lemmel EM, Pors-Nielsen S, Rizzoli R, Genant HK, Reginster JY. The Effects of Strontium Ranelate on the Risk of Vertebral Fracture in Women with Postmenopausal Osteoporosis. N Engl J Med. 2004; 350(5):459–468. [PubMed: 14749454]

21. Gallacher SJ, Dixon T. Impact of treatments for postmenopausal osteoporosis (bisphosphonates, parathyroid hormone, strontium ranelate, and denosumab) on bone quality: a systematic review. Calcif Tissue Int. 2010; 87(6):469–484. [PubMed: 20872215]

22. Tie D, Guan R, Liu H, Cipriano A, Liu Y, Wang Q, Huang Y, Hort N. An in vivo study on the metabolism and osteogenic activity of bioabsorbable Mg–1Sr alloy. Acta Biomater. 2016; 29:455–467. [PubMed: 26577986]

23. Kirkpatrick CJ, Mittermayer C. Theoretical and practical aspects of testing potential biomaterials in vitro. J Mater Sci: Mater Med. 1990; 1(1):9–13.

24. Cipriano AF, Sallee A, Guan RG, Zhao ZY, Tayoba M, Sanchez J, Liu H. Investigation of magnesium–zinc–calcium alloys and bone marrow derived mesenchymal stem cell response in direct culture. Acta Biomater. 2015; 12(1):298–321. [PubMed: 25449917]

25. Witte F, Fischer J, Nellesen J, Crostack HA, Kaese V, Pisch A, Beckmann F, Windhagen H. In vitro and in vivo corrosion measurements of magnesium alloys. Biomaterials. 2006; 27(7):1013–1018. [PubMed: 16122786]

26. Kirkland NT, Birbilis N, Staiger MP. Assessing the corrosion of biodegradable magnesium implants: A critical review of current methodologies and their limitations. Acta Biomater. 2012; 8(3):925–936. [PubMed: 22134164]

27. Sanchez AHM, Luthringer BJC, Feyerabend F, Willumeit R. Mg and Mg alloys: How comparable are in vitro and in vivo corrosion rates? A review. Acta Biomater. 2015; 13:16–31. [PubMed: 25484334]

28. Xin Y, Hu T, Chu PK. In vitro studies of biomedical magnesium alloys in a simulated physiological environment: A review. Acta Biomater. 2011; 7(4):1452–1459. [PubMed: 21145436]

29. Liu H. The effects of surface and biomolecules on magnesium degradation and mesenchymal stem cell adhesion. J Biomed Mater Res, Part A. 2011; 99(2):249–260.

30. Johnson I, Perchy D, Liu H. In vitro evaluation of the surface effects on magnesium-yttrium alloy degradation and mesenchymal stem cell adhesion. J Biomed Mater Res, Part A. 2012; 100A(2): 477–485.

31. Johnson I, Liu H. A study on factors affecting the degradation of magnesium and a magnesium-yttrium alloy for biomedical applications. PLoS One. 2013; 8(6):e65603. [PubMed: 23799028]

32. Rickard DJ, Sullivan TA, Shenker BJ, Leboy PS, Kazhdan I. Induction of Rapid Osteoblast Differentiation in Rat Bone Marrow Stromal Cell Cultures by Dexamethasone and BMP-2. Dev Biol. 1994; 161(1):218–228. [PubMed: 8293874]

33. Fischer J, Pröfrock D, Hort N, Willumeit R, Feyerabend F. Reprint of: Improved cytotoxicity testing of magnesium materials. Mater Sci Eng, B. 2011; 176(20):1773–1777.

34. Cipriano AF, De Howitt N, Gott SC, Miller CT, Rao MP, Liu H. Bone Marrow Stromal Cell Adhesion and Morphology on Micro- and Sub-Micropatterned Titanium. J Biomed Nanotechnol. 2014; 10(4):660–668. [PubMed: 24734518]

35. Larsen LB, Madsen JE, Høiness PR, Øvre S. Should Insertion of Intramedullary Nails for Tibial Fractures Be With or Without Reaming?: A Prospective, Randomized Study With 3. 8 Years' Follow-up. Journal of Orthopaedic Trauma. 2004; 18(3):144–149. [PubMed: 15091267]

36. Rammelt S, Illert T, Bierbaum S, Scharnweber D, Zwipp H, Schneiders W. Coating of titanium implants with collagen, RGD peptide and chondroitin sulfate. Biomaterials. 2006; 27(32):5561–5571. [PubMed: 16879866]

37. Otto TE, Patka P, Haarman HJTM, Klein CPAT, Vriesde R. Intramedullary bone formation after polylactic acid wire implantation. J Mater Sci: Mater Med. 1994; 5(6–7):407–410.

38. De Aza PN, Luklinska ZB, Santos C, Guitian F, De Aza S. Mechanism of bone-like formation on a bioactive implant in vivo. Biomaterials. 2003; 24(8):1437–1445. [PubMed: 12527285]

39. Kraus T, Fischerauer SF, Hänzi AC, Uggowitzer PJ, Löffler JF, Weinberg AM. Magnesium alloys for temporary implants in osteosynthesis: in vivo studies of their degradation and interaction with bone. Acta Biomater. 2012; 8(3):1230–1238. [PubMed: 22107870]

40. Erdmann N, Angrisani N, Reifenrath J, Lucas A, Thorey F, Bormann D, Meyer-Lindenberg A. Biomechanical testing and degradation analysis of MgCa0.8 alloy screws: A comparative in vivo study in rabbits. Acta Biomater. 2011; 7(3):1421–1428. [PubMed: 21050898]

41. Hofstetter J, Martinelli E, Pogatscher S, Schmutz P, Povoden-Karadeniz E, Weinberg AM, Uggowitzer PJ, Löffler JF. Influence of trace impurities on the in vitro and in vivo degradation of biodegradable Mg–5Zn–0.3Ca alloys. Acta Biomater. 2015; 23:347–353. [PubMed: 25983315]

42. Gu XN, Xie XH, Li N, Zheng YF, Qin L. In vitro and in vivo studies on a Mg–Sr binary alloy system developed as a new kind of biodegradable metal. Acta Biomater. 2012; 8(6):2360–2374. [PubMed: 22387336]

43. Han P, Cheng P, Zhang S, Zhao C, Ni J, Zhang Y, Zhong W, Hou P, Zhang X, Zheng Y, Chai Y. In vitro and in vivo studies on the degradation of high-purity Mg (99.99wt. %) screw with femoral intracondylar fractured rabbit model. Biomaterials. 2015; 64:57–69. [PubMed: 26117658]

44. Wang J, Jiang H, Bi Y, Sun Je, Chen M, Liu D. Effects of gas produced by degradation of Mg–Zn–Zr Alloy on cancellous bone tissue. Mater Sci Eng, C. 2015; 55:556–561.

45. Butz F, Ogawa T, Chang TL, Nishimura I. Three-dimensional bone-implant integration profiling using micro-computed tomography. Int J Oral Maxillofac Implants. 2006; 21(5):687–695. [PubMed: 17066629]

46. Bernhardt R, van den Dolder J, Bierbaum S, Beutner R, Scharnweber D, Jansen J, Beckmann F, Worch H. Osteoconductive modifications of Ti-implants in a goat defect model: characterization of bone growth with SR μCT and histology. Biomaterials. 2005; 26(16):3009–3019. [PubMed: 15603796]

47. Morinaga K, Kido H, Sato A, Watazu A, Matsuura M. Chronological Changes in the Ultrastructure of Titanium-Bone Interfaces: Analysis by Light Microscopy, Transmission Electron Microscopy,

and Micro-Computed Tomography. Clinical Implant Dentistry and Related Research. 2009; 11(1): 59–68. [PubMed: 18384402]

48. Sheng MHC, Baylink DJ, Beamer WG, Donahue LR, Lau KHW, Wergedal JE. Regulation of bone volume is different in the metaphyses of the femur and vertebra of C3H/HeJ and C57BL/6J mice. Bone. 2002; 30(3):486–491. [PubMed: 11882462]

49. Gruber HE. Adaptations of Goldner's Masson Trichrome Stain for the Study of Undecalcified Plastic Embedded Bone. Biotech Histochem. 1992; 67(1):30–34. [PubMed: 1617000]

50. Nguyen TY, Liew CG, Liu H. An In Vitro Mechanism Study on the Proliferation and Pluripotency of Human Embryonic Stems Cells in Response to Magnesium Degradation. PLoS One. 2013; 8(10):e76547. [PubMed: 24146887]

51. Lai YM, Qin L, Hung VWY, Chan KM. Regional differences in cortical bone mineral density in the weight-bearing long bone shaft—A pQCT study. Bone. 2005; 36(3):465–471. [PubMed: 15777653]

52. Chatterjee S. Artefacts in histopathology. J Oral Maxillofac Pathol. 2014; 18:S111–S116. [PubMed: 25364159]

53. Mavrogenis A, Dimitriou R, Parvizi J, Babis G. Biology of implant osseointegration. J Musculoskelet Neuronal Interact. 2009; 9(2):61–71. [PubMed: 19516081]

54. Kirkland NT, Lespagnol J, Birbilis N, Staiger MP. A survey of bio-corrosion rates of magnesium alloys. Corros Sci. 2010; 52(2):287–291.

55. Seitz JM, Collier K, Wulf E, Bormann D, Angrisani N, Meyer-Lindenberg A, Bach FW. The effect of different sterilization methods on the mechanical strength of magnesium based implant materials. Adv Eng Mater. 2011; 13(12):1146–1151.

56. Brar HS, Wong J, Manuel MV. Investigation of the mechanical and degradation properties of Mg–Sr and Mg–Zn–Sr alloys for use as potential biodegradable implant materials. Journal of the Mechanical Behavior of Biomedical Materials. 2012; 7(0):87–95. [PubMed: 22340688]

57. Li H, Peng Q, Li X, Li K, Han Z, Fang D. Microstructures, mechanical and cytocompatibility of degradable Mg–Zn based orthopedic biomaterials. Mater Eng. 2014; 58(0):43–51.

58. Aljarrah M, Aghaulor U, Medraj M. Thermodynamic assessment of the Mg–Zn–Sr system. Intermetallics. 2007; 15(2):93–97.

59. Johnson I, Perchy D, Liu HN. In vitro evaluation of the surface effects on magnesium-yttrium alloy degradation and mesenchymal stem cell adhesion. J Biomed Mater Res, Part A. 2012; 100A(2): 477–485.

60. Walker J, Shadanbaz S, Kirkland NT, Stace E, Woodfield T, Staiger MP, Dias GJ. Magnesium alloys: Predicting in vivo corrosion with in vitro immersion testing. J Biomed Mater Res, Part B. 2012; 100B(4):1134–1141.

61. Willumeit R, Feyerabend F, Huber N. Magnesium degradation as determined by artificial neural networks. Acta Biomater. 2013; 9(10):8722–8729. [PubMed: 23470548]

62. Johnson I, Jiang W, Liu H. The Effects of Serum Proteins on Magnesium Alloy Degradation in Vitro. Sci Rep. 2017; 7(1):14335. [PubMed: 29084971]

63. Li Z, Gu X, Lou S, Zheng Y. The development of binary Mg–Ca alloys for use as biodegradable materials within bone. Biomaterials. 2008; 29(10):1329–1344. [PubMed: 18191191]

64. Kokubo T. Formation of biologically active bone-like apatite on metals and polymers by a biomimetic process. Thermochim Acta. 1996; 280–281:479–490.

65. Zhang S, Zhang X, Zhao C, Li J, Song Y, Xie C, Tao H, Zhang Y, He Y, Jiang Y, Bian Y. Research on an Mg–Zn alloy as a degradable biomaterial. Acta Biomater. 2010; 6(2):626–640. [PubMed: 19545650]

66. Willbold E, Kaya AA, Kaya RA, Beckmann F, Witte F. Corrosion of magnesium alloy AZ31 screws is dependent on the implantation site. Mater Sci Eng, B. 2011; 176(20):1835–1840.

67. Xu L, Yu G, Zhang E, Pan F, Yang K. In vivo corrosion behavior of Mg-Mn-Zn alloy for bone implant application. J Biomed Mater Res, Part A. 2007; 83A(3):703–711.

68. Zhang E, Xu L, Yu G, Pan F, Yang K. In vivo evaluation of biodegradable magnesium alloy bone implant in the first 6 months implantation. J Biomed Mater Res, Part A. 2009; 90(3):882–893.

69. Banai S, Haggroth L, Epstein SE, Casscells W. Influence of extracellular magnesium on capillary endothelial cell proliferation and migration. Circ Res. 1990; 67(3):645–650. [PubMed: 1697793]

70. Liu C, Fu X, Pan H, Wan P, Wang L, Tan L, Wang K, Zhao Y, Yang K, Chu PK. Biodegradable Mg-Cu alloys with enhanced osteogenesis, angiogenesis, and long-lasting antibacterial effects. Sci Rep. 2016; 6:27374. [PubMed: 27271057]

71. Noronha LJ, Matuschak GM. Magnesium in critical illness: metabolism, assessment, and treatment. Intensive Care Med. 2002; 28(6):667–679. [PubMed: 12107669]

72. Feyerabend F, Fischer J, Holtz J, Witte F, Willumeit R, Drücker H, Vogt C, Hort N. Evaluation of short-term effects of rare earth and other elements used in magnesium alloys on primary cells and cell lines. Acta Biomater. 2010; 6(5):1834–1842. [PubMed: 19800429]

73. Marie P, Ammann P, Boivin G, Rey C. Mechanisms of action and therapeutic potential of strontium in bone. Calcif Tissue Int. 2001; 69(3):121–129. [PubMed: 11683526]

74. Winek C, Buehler E. Intravenous toxicity of zinc pyridinethione and several zinc salts. Toxicol Appl Pharmacol. 1966; 9(2):269–273. [PubMed: 4961359]

75. Kroes R, Den Tonkelaar E, Minderhoud A, Speijers G, Vonk-Visser D, Berkvens J, Van Esch G. Short-term toxicity of strontium chloride in rats. Toxicology. 1977; 7(1):11–21. [PubMed: 841579]

76. Wang JL, Mukherjee S, Nisbet DR, Birbilis N, Chen XB. In vitro evaluation of biodegradable magnesium alloys containing micro-alloying additions of strontium, with and without zinc. J Mater Chem B. 2015; 3(45):8874–8883.

77. Witte F, Kaese V, Haferkamp H, Switzer E, Meyer-Lindenberg A, Wirth CJ, Windhagen H. In vivo corrosion of four magnesium alloys and the associated bone response. Biomaterials. 2005; 26(17): 3557–3563. [PubMed: 15621246]

78. Witte F, Ulrich H, Palm C, Willbold E. Biodegradable magnesium scaffolds: Part II: Peri-implant bone remodeling. J Biomed Mater Res, Part A. 2007; 81A(3):757–765.

79. Xu L, Pan F, Yu G, Yang L, Zhang E, Yang K. In vitro and in vivo evaluation of the surface bioactivity of a calcium phosphate coated magnesium alloy. Biomaterials. 2009; 30(8):1512–1523. [PubMed: 19111896]

80. Wang YB, Xie XH, Li HF, Wang XL, Zhao MZ, Zhang EW, Bai YJ, Zheng YF, Qin L. Biodegradable CaMgZn bulk metallic glass for potential skeletal application. Acta Biomater. 2011; 7(8):3196–3208. [PubMed: 21571105]

81. Witte F, Ulrich H, Rudert M, Willbold E. Biodegradable magnesium scaffolds: Part 1: Appropriate inflammatory response. J Biomed Mater Res, Part A. 2007; 81A(3):748–756.

82. Sun, Je, Wang, J., Jiang, H., Chen, M., Bi, Y., Liu, D. In vivo comparative property study of the bioactivity of coated Mg–3Zn–0.8Zr alloy. Mater Sci Eng, C. 2013; 33(6):3263–3272.
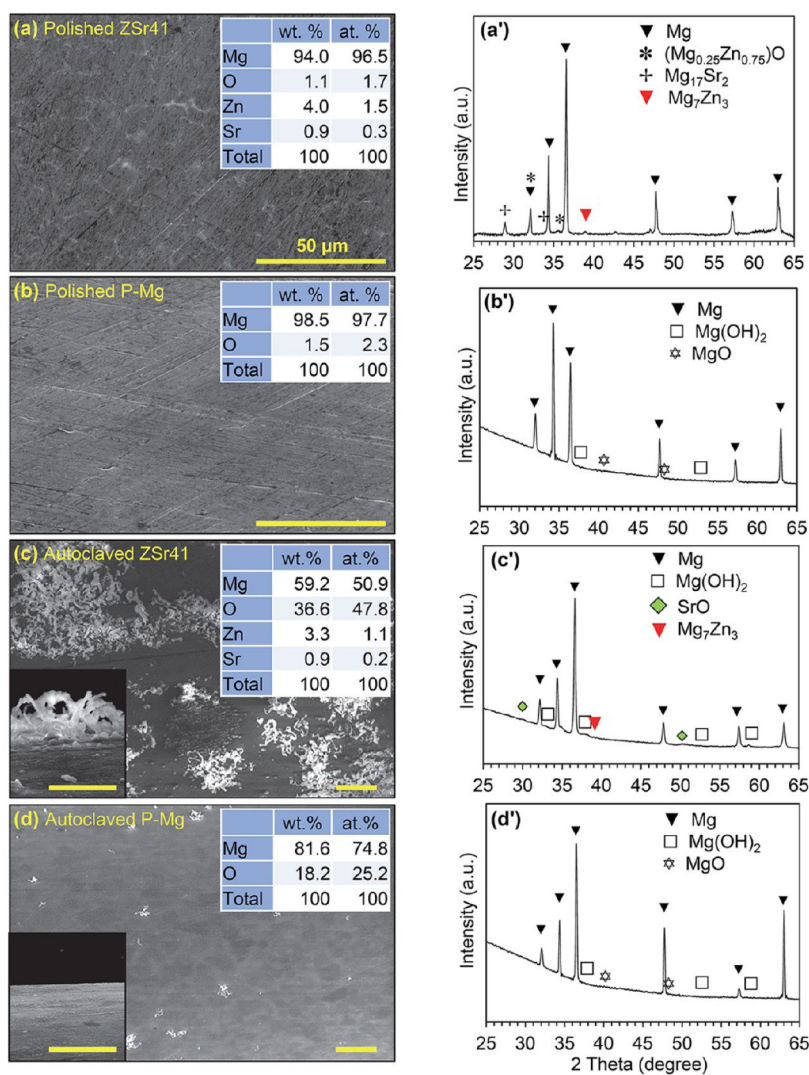
Figure 1.
Characterization of ZSr41 and P–Mg pins. SEM images and surface elemental composition quantified through EDS area analysis, and corresponding X-ray diffraction patterns, respectively, for (a and a′) polished ZSr41, (b and b′) polished P–Mg, (c and c′) autoclaved ZSr41, and (d and d′) autoclaved P–Mg. SEM insets in panels c and d are side-views of the surfaces respective to each sample. Original magnification: (a and b) 1000×, (c and d) 160×, and insets in panels c and d, 500×. Scale bar = 50 μm for all images.
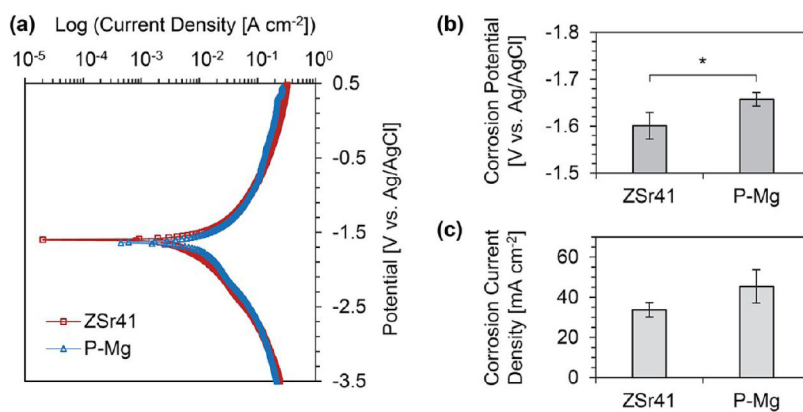
Figure 2.
Electrochemical testing results of ZSr41 and P–Mg pins. (a) Representative potentiodynamic polarization curves of polished metallic samples using r-SBF at 37 °C as the electrolyte and (b) corrosion potential and (c) corrosion current density obtained from Tafel extrapolation (ASTM G102-89) of potentiodynamic polarization curves; values are mean ± SD, $n = 3$, *$p < 0.05$.
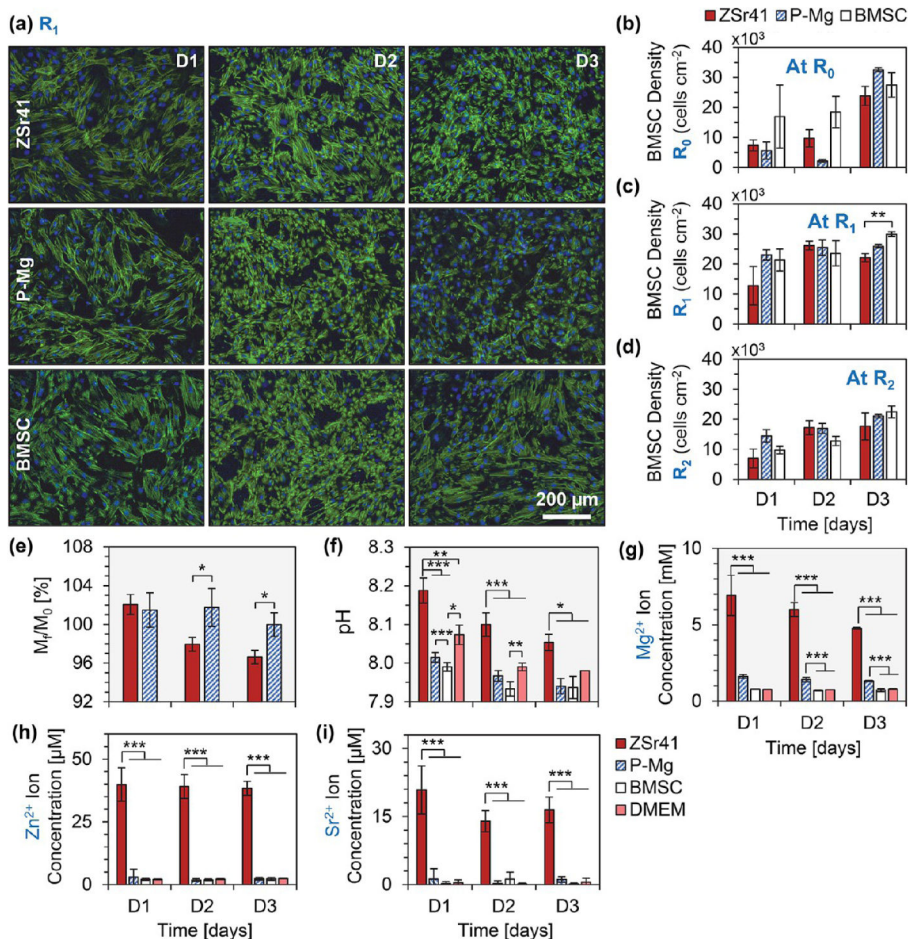
Figure 3.

In vitro cytocompatibility and degradation of ZSr41 and P–Mg pins in exposure culture with BMSCs during a 3-day period (D1, D2, D3). At each day interval, culture media was collected, measured, and replaced with fresh media. BMSC and DMEM designate cells-only positive control and blank media reference groups, respectively. (a) Representative fluorescence images of BMSCs adhered on the plate location R_1 (3.5 mm from the well center) after exposure culture with the pins. Blue: DAPI stained nuclei. Green: Alexa Fluor 488 phalloidin-stained cytoskeleton. Scale bar = 200 μm for all images. Original magnification: 10×. (b–d) BMSC adhesion density on culture plates on the well center (R_0), 3.5 mm from well center (R_1), and 7.0 mm from well center (R_2), respectively. (e) Percent final mass (M_f) relative to initial mass of the pins (M_0). (f) pH of BMSC culture media incubated with pins. (g–i) Mg^{2+}, Zn^{2+}, and Sr^{2+} ion concentration, respectively, in BMSC culture media incubated with the pins. Values in panels b–d are average ± SE and those in panels e–i are average ± SD. (b–e) $n = 3$ for all groups and time points, and (f–i) $n = 9$ at D1, $n = 6$ at D2, $n = 3$ at D3 for all groups. *$p < 0.05$, **$p < 0.01$, ***$p < 0.001$.
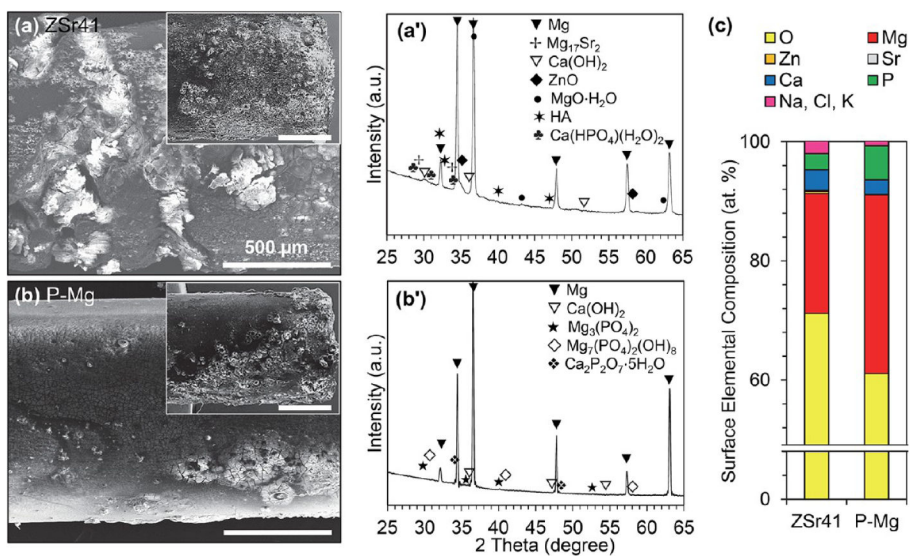
Figure 4.
Characterization of ZSr41 and P–Mg pins after *in vitro* degradation in exposure culture with BMSCs for a 3-day period. SEM images and corresponding X-ray diffraction patterns for (a and a′) ZSr41 and (b and b′) P–Mg, respectively. SEM insets in panels a and b represent degradation that occurred at the end of pins. Original magnification: 65×. Scale bar = 500 μm for all images. (c) Surface elemental composition (at. %) quantified through EDS area analysis on panels a and b at 65× magnification.
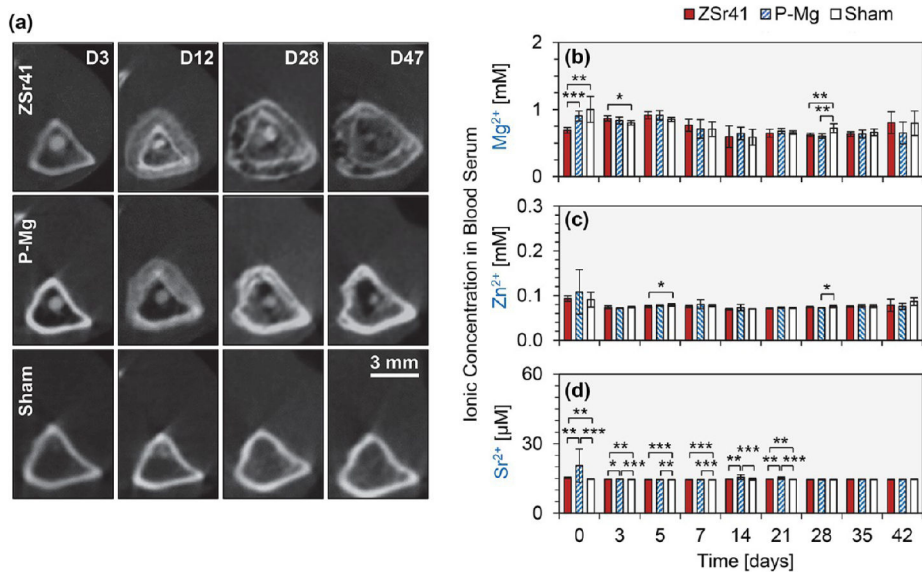
Figure 5.
In vivo degradation of ZSr41 alloy and P–Mg intramedullary pins over an implantation period of 47 days in rat tibia. Sham designates the control group with intramedullary cavity but no pin implant. (a) Representative transverse 2D μCT images obtained from the proximal tibia (at the mid-diaphysis 5 mm from the tibial plateau) with implanted intramedullary pins in 12-week old Sprague–Dawley rats. Scale bar = 3 mm. (b–d) Mg^{2+}, Zn^{2+}, and Sr^{2+} ion concentration, respectively, in rat blood during implantation of intramedullary pins. Values are average ± SD; $n = 6$ for all groups during all time points. $*p < 0.05$, $**p < 0.01$, $***p < 0.001$.
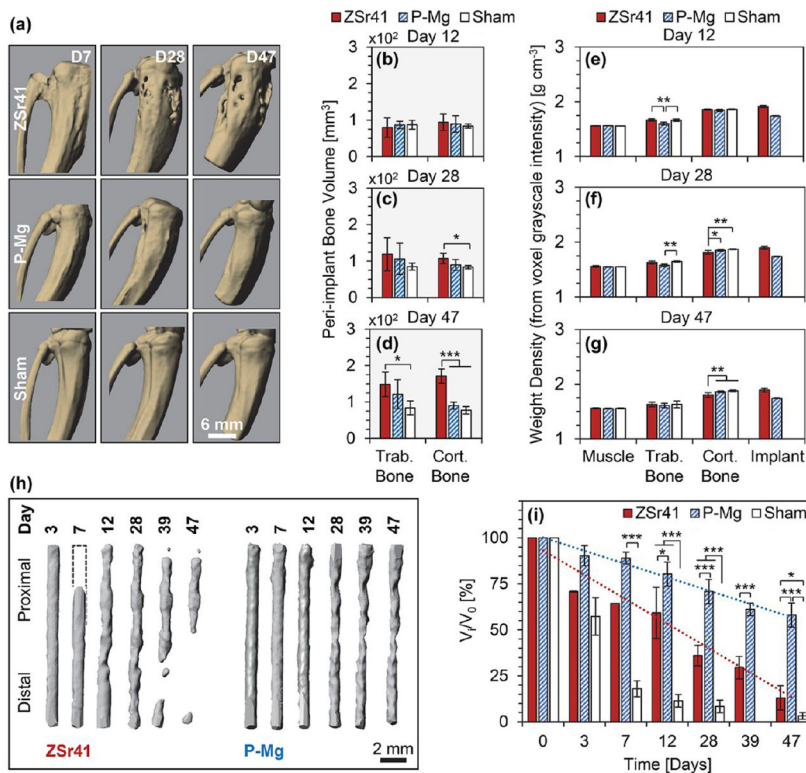
Figure 6.
Bone remodeling around the proximal tibia in response to the degradation of ZSr41 and P–Mg intramedullary pins throughout an implantation period of 47 days. Images of 3D structures were all reconstructed from μCT data in IMARIS using the volume of interest (VOI) technique with an optimized threshold based on statistical analysis. Sham designates the control group with intramedullary cavity but no intramedullary pin. (a) Representative 3D images of the VOIs around proximal tibia at 7, 28, and 47 days postsurgery. (b–d) Volume of the trabecular and cortical peri-implant bone regions of the proximal tibial diaphysis (defined between tibial tuberosity and 12.82 ± 50 mm distally from tibial plateau) at (b) 12, (c) 28, and (d) 47 days postsurgery. (e–g) Weight density (not bone mineral density) of muscle, and trabecular and cortical peri-implant bone regions specified in panels b–d. The theoretical physical densities of ZSr41 (1.90 g cm^{-3}) and P–Mg (1.74 g cm^{-3}) and corresponding voxel grayscale intensity values at day 0 for the pins were used as calibration phantoms to calculate the weight density for each VOI. (h) Representative 3D images of the ZSr41 and P–Mg intramedullary pins reconstructed at select time points postimplantation. The dotted line in the 3D image of ZSr41 pin at day 7 outlines a missing region of the implant caused by a misaligned μCT scan. Scale bar = 2 mm for all images. (i) Percent implant volume at each time point (V_i; $i = 0, 3, 7, 12, 28, 39$, and 47 days) relative to initial volume of each implant (V_0). The volume for Sham indicates the volume of the predrilled cavity. Values are mean $\pm$ SD; please see Table 1 for sample size for each group at each time point. $*p < 0.05$, $**p < 0.01$, $***p < 0.001$.
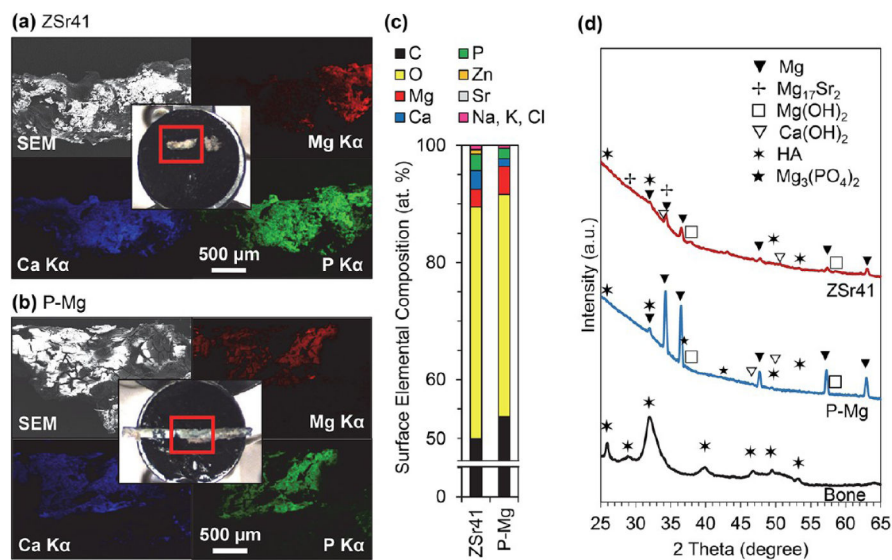
Figure 7.
Characterization of residual ZSr41 and P–Mg intramedullary pins dissected after implantation in rat tibiae for 47 days. (a) and (b) Montage containing optical image of dissected pin, SEM images, and corresponding surface elemental distribution maps (Mg, Ca, and P) for (a) ZSr41 and (b) P–Mg. Original magnification: 50×. Scale bar = 500 μm for all SEM images and EDS maps. Red rectangles in the optical images indicate regions of implants for SEM and EDS analyses. (c) Surface elemental composition (at. %) quantified through EDS area analysis on SEM images in panels a and b at 50× magnification. (d) X-ray diffraction patterns of the surface of the residual ZSr41 and P–Mg implants, along with diffraction pattern for pulverized 19-week old rat tibia.
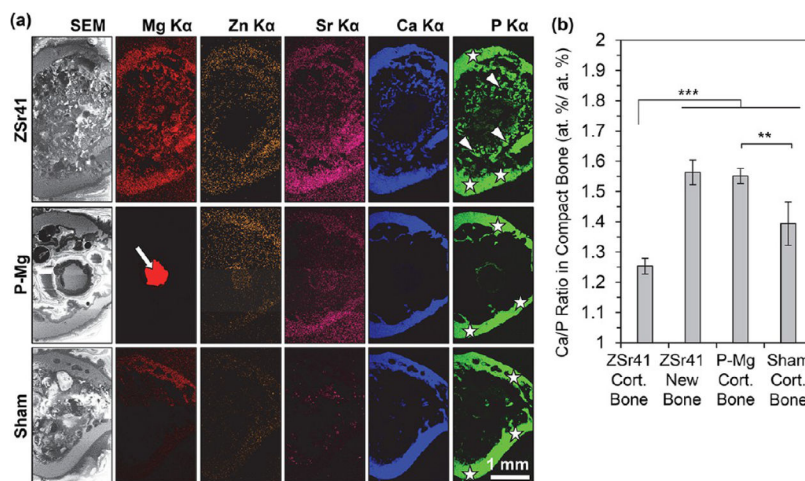
Figure 8.
Elemental mapping analyses on epoxy-embedded cross sections obtained transversely at the mid-diaphysis 5 mm from the tibial plateau with implanted intramedullary pins at 47 days postsurgery. Sham designates the control group with intramedullary cavity but no intramedullary pin. (a) Montage containing composite SEM images and corresponding surface elemental distribution maps of Mg, Zn, Sr, Ca, and P for the transverse cross sections. At this anatomical location, the ZSr41 implant was completely degraded and resorbed, whereas a residual P–Mg implant remained as indicated by the white arrow in Mg Kα map for P–Mg. Original magnification: 50×. Scale bar = 1 mm for all SEM images and EDS maps. (b) Quantification of Ca/P (atomic %/atomic %) ratio from EDS analyses at the cortical bone regions indicated by white stars in P Kα distribution maps in (a). ZSr41 New Bone designates newly formed bone fractions in the peri-implant bone tunnel (indicated with white arrowheads). Values are average ± SD; $n = 3$ for all groups. **$p < 0.01$, ***$p < 0.001$.
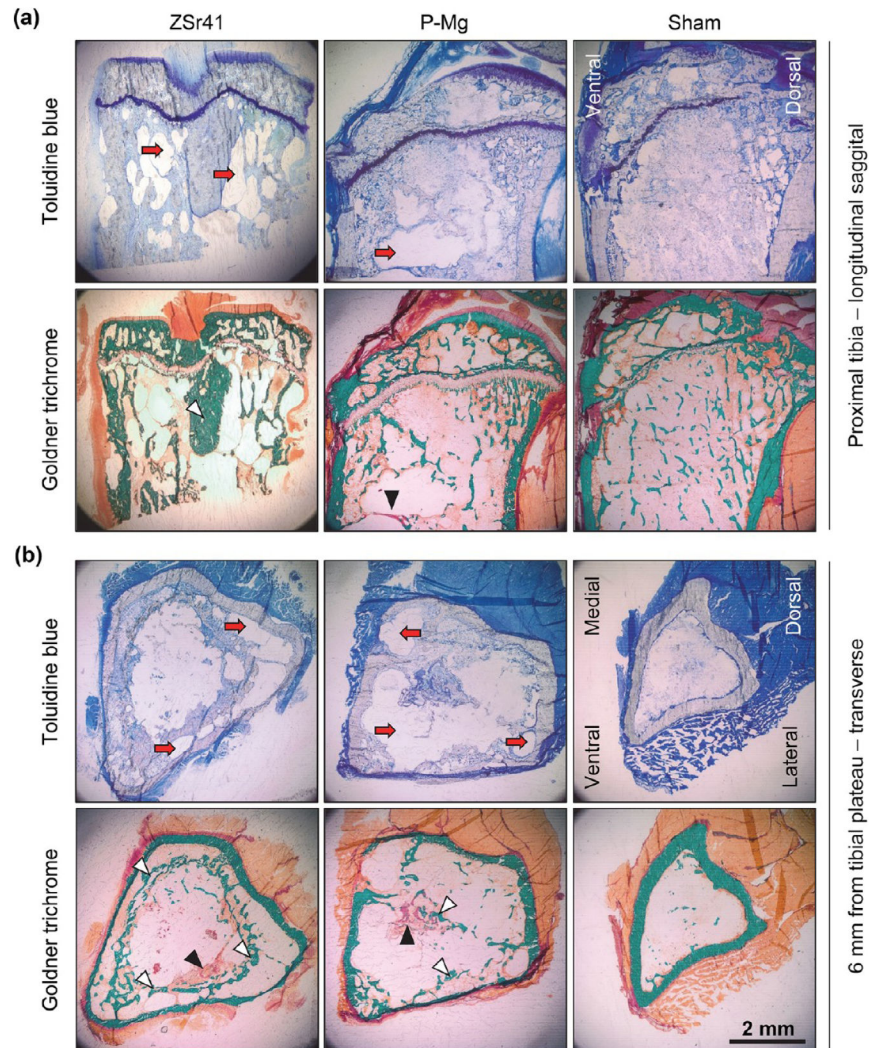
Figure 9.
Representative optical images of plastic-embedded thin histology sections of undecalcified bone tissue harvested at 47 days postsurgery. Sections were cut: (a) longitudinally along the sagittal plane of the proximal tibia, and (b) transversally at the mid-diaphysis 6 mm from the tibial plateau. Sections were stained with toluidine blue (blue = cell structure, purple = collagen, and gray = bone) and Goldner Masson trichrome (green = mineralized bone, red = unmineralized osteoid, and brownish-gray = bone marrow cells). Images were obtained at an original magnification of 2.5×; scale bar = 2 mm for all images. White arrowheads indicate new bone formation; black arrowheads indicate unmineralized osteoid; and, red arrows indicate hydrogen gas-induced cavities and absence of bone marrow cells.
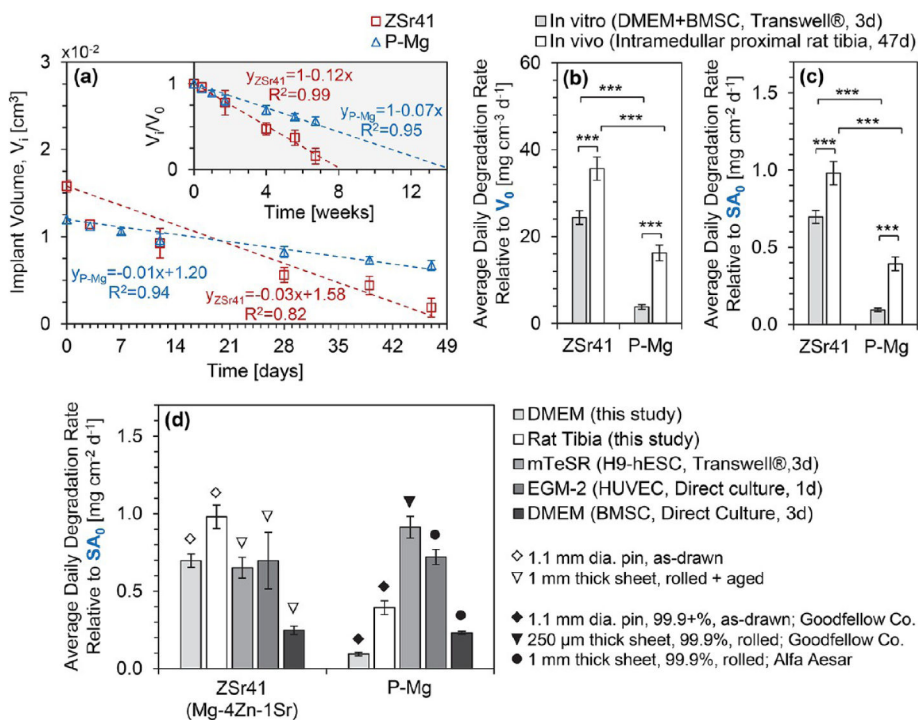
Figure 10.
Analyses of the in vitro and in vivo degradation of ZSr41 alloys. (a) Intramedullary pin volume during the implantation in the rat tibia as a function of time in days. Inset in panel a represents the ratio of implant volume (V_i) at each time point relative to the initial implant volume (V_0) as a function of time in weeks. (b and c) Comparison of the average daily in vitro and in vivo degradation rates (mass loss rates) of ZSr41 and P–Mg pins relative to the (b) initial volume of the pins (V_0) or (c) initial surface area of the pins (SA_0). The average daily in vitro degradation rates were calculated from Mg^{2+} ion concentration in media and averaged over a 3-day period. The average daily in vivo degradation rates were calculated from implant volume obtained from reconstructed 3D μCT data and averaged over a 47 day period. Values are mean ± SD, $n = 3$ for in vitro, and $n = 5$ for in vivo; ***$p < 0.001$. (d) Average daily in vitro and in vivo degradation rates per unit SA_0 of ZSr41 and P–Mg pins from this study in comparison with the values from previously published in vitro studies. [8,10,11] The color of each bar designates the model system (i.e., media type, cell type, culture configuration, culture time) and the icon above each bar designates material properties (i.e., geometry, purity, processing, and for Mg, commercial source).

Table 1

Designated Animals Per Group and Data Collected from Each Specimen to Investigate the in Vivo Degradation of ZSr41 Intramedullary Pins and Mg Control and Associated Biological Responses

rat ID	group	blood collected at all time points	time points (day no.) with complete μCT scans for 3D reconstruction and analysis of peri-implant bone	time points (day no.) with complete μCT scans for 3D reconstruction and analysis of implant	destructive testing technique post mortem
1	P–Mg	yes	12, 28, 39	3, 7, 12, 28, 39, 47	implant surface analysis (SEM/EDS/XRD)
2	P–Mg	yes	12, 28, 39	–, –, 12, 28, 39, 47	implant surface analysis (SEM/EDS/XRD)
3	P–Mg	yes	12, 28, 39	3, 7, 12, 28, 39, 47	histology
4	P–Mg	yes	N/A[a]	N/A[a]	N/A[a]
5	P–Mg	yes	12, 28, 39	–, 7, 12, 28, 39, 47	histology
6	P–Mg	yes	–, 28, 39	–, 7, –, 28, 39, 47	bone-implant interface (SEM and EDS elemental mapping)
7	ZSr41	yes	12, 28, –	3, –, 12, 28, 39, 47	histology
8	ZSr41	yes	12, 28, 39	–, –, 12, 28, 39, 47	implant surface analysis (SEM/EDS/XRD)
9	ZSr41	yes	N/A[a]	N/A[a]	N/A[a]
10	ZSr41	yes	12, 28, 39	–, –, 12, 28, 39, 47	histology
11	ZSr41	yes	12, 28, 39	–, –, 12, 28, 39, 47	bone-implant interface (SEM and EDS elemental mapping)
12	ZSr41	yes	–, 28, 39	3, 7, –, 28, –, 47	implant surface analysis (SEM/EDS/XRD)
13	Sham	yes	–, 28, 39	3, –, –, 28, –, 47	bone-implant interface (SEM and EDS elemental mapping)
14	Sham	yes	12, 28, –	3, 7, 12, 28, –, 47	histology
15	Sham	yes	–, 28, 39	3, 7, –, 28, –, 47	histology
16	Sham	yes	12, 28, 39	3, 7, 12, 28, –, 47	histology
17	Sham	yes	12, 28, 39	–, –, 12, 28, –, 47	histology
18	Sham	yes	12, 28, 39	3, 7, 12, 28, –, 47	histology

[a]N/A: The pin implant was placed partially outside of bone tunnel and data were not used for analyses.

Table 2

Results of Statistical Analyses on Measured Mg^{2+}, Sr^{2+}, and Zn^{2+} Ionic Concentrations in the Collected Blood of Rats

ion	time point	family-wise test	family-wise statistics summary	post hoc pairwise comparison (measured values, mean ± SD)	significance
Mg^{2+} [mM]	D0	ANOVA (w/o homogeny. variance)	$F_{(2, 8)} = 22.806$, $p = 4.168 \times 10^{-4}$	ZSr41 (0.69 ± 0.04) < P–Mg (0.91 ± 0.07)	$p < 0.001$
				ZSr41 (0.69 ± 0.04) < Sham (1.00 ± 0.19)	$p < 0.01$
	D3	ANOVA	$F_{(2, 15)} = 3.809$, $p = 4.59 \times 10^{-2}$	ZSr41 (0.87 ± 0.04) > Sham (0.80 ± 0.03)	$p < 0.05$
	D28	ANOVA	$F_{(2, 15)} = 11.457$, $p = 9.452 \times 10^{-4}$	ZSr41 (0.62 ± 0.02) < Sham (0.72 ± 0.07)	$p < 0.01$
				P–Mg (0.60 ± 0.03) < Sham (0.72 ± 0.07)	$p < 0.01$
Zn^{2+} [mM]	D5	ANOVA	$F_{(2, 15)} = 4.601$, $p = 2.766 \times 10^{-2}$	ZSr41 (75.49 ± 2.32) < Sham (79.35 ± 2.89)	$p < 0.05$
	D28	ANOVA	$F_{(2, 15)} = 4.722$, $p = 2.567 \times 10^{-2}$	P–Mg (72.55 ± 1.03) < Sham (75.49 ± 2.55)	$p < 0.05$
Sr^{2+} [µM]	D0	Kruskal–Wallis	$X2_{(2, N = 18)} = 14.749$, $p = 6.272 \times 10^{-4}$	P–Mg (20.54 ± 7.16) > Sham (14.74 ± 0.13)	$p < 0.001$
				ZSr41 (15.31 ± 0.33) < P–Mg (20.54 ± 7.16)	$p < 0.01$
				ZSr41 (15.31 ± 0.33) > Sham (14.74 ± 0.13)	$p < 0.05$
	D3	Kruskal–Wallis	$X2_{(2, N = 18)} = 13.345$, $p = 1.265 \times 10^{-3}$	P–Mg (14.71 ± 0.08) > Sham (14.55 ± 0.05)	$p < 0.001$
				ZSr41 (14.64 ± 0.02) > Sham (14.55 ± 0.05)	$p < 0.01$
				ZSr41 (14.64 ± 0.02) < P–Mg (14.71 ± 0.08)	$p < 0.05$
	D5	ANOVA	$F_{(2, 15)} = 14.526$, $p = 3.097 \times 10^{-4}$	ZSr41 (14.51 ± 0.02) > Sham (14.46 ± 0.02)	$p < 0.001$
				P–Mg (14.50 ± 0.01) > Sham (14.46 ± 0.02)	$p < 0.01$
	D7	ANOVA	$F_{(2, 15)} = 21.873$, $p = 3.583 \times 10^{-5}$	ZSr41 (14.50 ± 0.02) > Sham (14.43 ± 0.01)	$p < 0.001$
				P–Mg (14.48 ± 0.02) > Sham (14.43 ± 0.01)	$p < 0.001$
	D14	Kruskal–Wallis	$X2_{(2, N = 18)} = 10.152$, $p = 6.245 \times 10^{-3}$	P–Mg (15.58 ± 1.00) > Sham (14.72 ± 0.46)	$p < 0.001$
				ZSr41 (14.68 ± 0.04) < P–Mg (15.58 ± 1.00)	$p < 0.01$
	D21	Kruskal–Wallis	$X2_{(2, N = 18)} = 15.158$, $p = 5.111 \times 10^{-4}$	P–Mg (15.15 ± 0.53) > Sham (14.55 ± 0.03)	$p < 0.001$
				ZSr41 (14.66 ± 0.03) < P–Mg (15.15 ± 0.53)	$p < 0.01$
				ZSr41 (14.66 ± 0.03) > Sham (14.55 ± 0.03)	$p < 0.01$